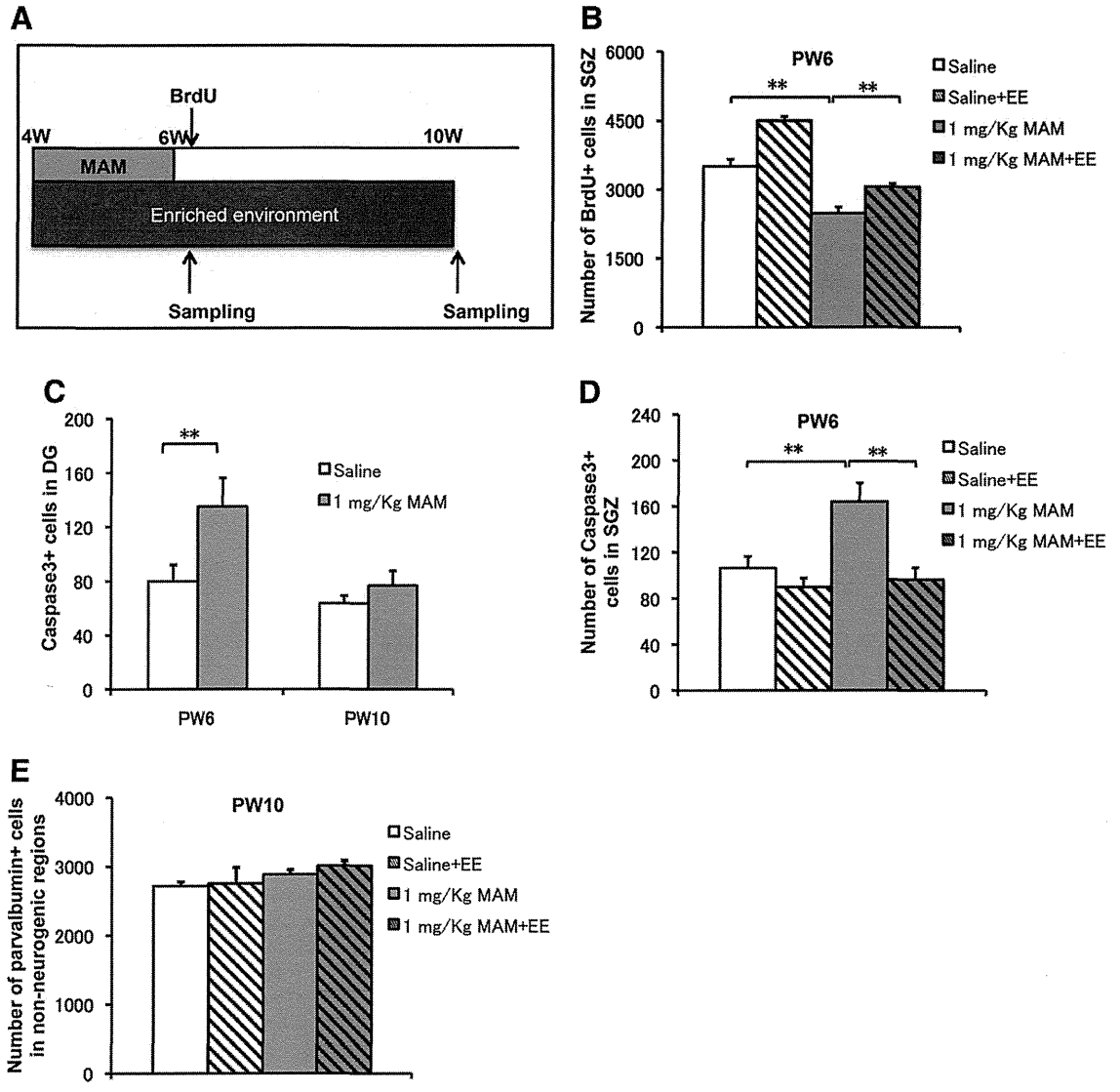

Figure 10. The effect of EE application on the proliferation of newborn cells and MAM-induced cell death. ***A***, Experimental design for MAM treatment, EE application during PW4–PW10, BrdU injection, and cellular analysis. ***B***, Cell proliferation in the DG, which was indicated by one pulse of BrdU incorporation (50 mg/kg) 2 h before sampling, was significantly decreased by MAM treatment (blue bar) compared with the saline group (open bar) ($F_{(1,10)} = 24.94531$, $p = 0.00054$ for MAM vs saline, $n = 6$ for each group). EE application increased the number of BrdU+ cells compared with MAM treatment ($F_{(1,10)} = 17.49274$, $p = 0.00127$ for MAM vs saline, $n = 6$ for saline and $n = 8$ for MAM group). ***C***, Consistently, the number of caspase3+ cells was increased immediately after MAM treatment at PW6 ($F_{(1,10)} = 5.09431$, $p = 0.04761$ for MAM vs saline, $n = 6$ for each group) and returned to the control level at PW10 ($F_{(1,10)} = 1.17259$, $p = 0.30429$ for MAM vs saline, $n = 6$ for each group) after a 4 week withdrawal from MAM treatment. ***D***, EE application from PW4 to PW6 effectively restored the number of caspase3+ cells to the control level at PW6 ($F_{(1,14)} = 12.2023$, $p = 0.00358$ for MAM vs saline, $n = 8$ samples for each group). ***E***, There were no differences in the numbers of PV+ cells in non-neurogenic regions between the saline and MAM groups or between the MAM and MAM with EE application groups at PW10 ($F_{(3,28)} = 1.08798$, $p = 0.37037$ for MAM vs saline, $n = 8$ samples for each group). $^*p < 0.05$; $^{**}p < 0.01$.

density of DCX+ cells in the saline-treated and MAM-treated groups in the DG at PW10 (Fig. 9*B*), which is consistent with the full rescue of BrdU+ granule cells (Fig. 1*C*). As expected, both the 4 and 6 week EE conditions increased the density of DCX+ cells in the DG (Fig. 9*B*). Therefore, an overall increase in immature neurons is the common effect of EE application, regardless of inclusion or exclusion of the 2 week MAM exposure period. In contrast to the above results regarding the density of newly generated immature neurons, there was a marked difference in the morphology of the DCX+ cells among these groups. We categorized DCX+ cells into two types according to their morphological characteristics (Fig. 9*C*): immature type A cells had no or very short vertical processes and did not reach into the molecular layer (Fig. 9*C*, arrowhead), whereas more mature type B cells had thick vertical dendritic processes that reached the molecular layer (Fig. 9*C*, arrow). The ratio of the number of B cells to the total number of DCX+ cells was significantly decreased in the MAM-treated group. This ratio was rescued by a 6 week EE application but not by the 4 week EE application (Fig. 9*D*). This result was in parallel with the above findings: PPI deficits were rescued by 6 week EE application but not 4 week EE application (Fig. 7*B*,*F*).

We also examined whether EE application for 6 weeks could rescue the MAM-induced deficits in GABAergic cells. The number of PV+ cells in the DG was significantly decreased in the MAM group compared with the saline group (Fig. 9*E*). As expected, the number of PV+ cells in the MAM-treated mice was restored by 6 week EE application but not by a 4 week EE application (Fig. 9*E*). It is noteworthy that there were no differences in the numbers of PV+ cells in the hippocampal non-neurogenic regions, including CA1, CA2, and CA3, either with or without EE application (Fig. 10*F*). This finding suggests that proper development of the GABAergic system in the DG during the defined

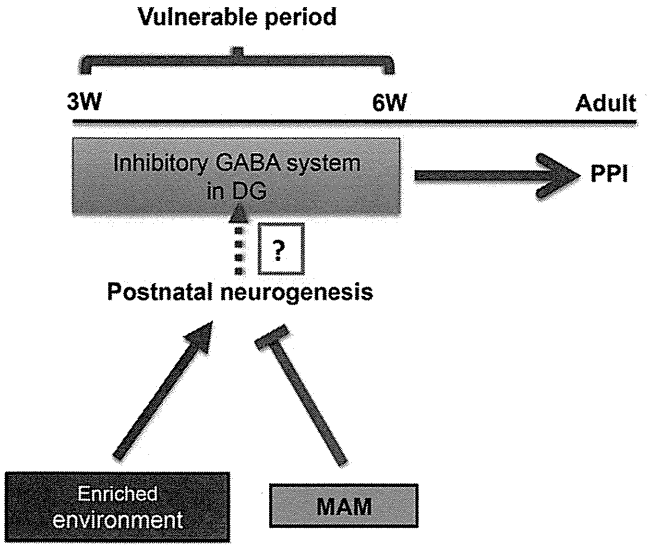

Figure 11. Graphical summary showing that the developmental intervention during vulnerable postnatal stage affects the PPI circuit establishment at adulthood. EE and MAM treatment before critical time point (PW6) may modulate the GABA inhibitory system by affecting the postnatal neurogenesis in the DG.

adolescent period is critical for the establishment of PPI responses.

To further test the association between decreased neurogenesis at adolescent stages and PPI deficits in early adulthood, we also examined the proliferation of newborn cells in the DG of mice treated with MAM and exposed to EE (Fig. 10*B*). An ANOVA analysis revealed that the decrease in BrdU+ cells in the DG at PW6 was partially rescued by EE application; there were significant differences between the MAM-plus-6-week-EE group and the MAM group (Fig. 10*B*). We also examined cell death by immunostaining for caspase3. The number of caspase3+ cells increased due to MAM treatment at PW6 and returned to the control level by PW10 (Fig. 10*C*). The increase in caspase3+ cells caused by MAM treatment was abolished at PW6 after a 2 week EE application (Fig. 10*D*). Consistent with rescued PPI, rescue of the morphological phenotypes of DCX+ cells and proliferation of newborn cells by EE application support our idea of a critical period, during which intact neurogenesis is associated with the amelioration of PPI deficits caused by environmental intervention.

Discussion

In the present study, we established a developmental model of neuropsychiatric disorders by using the antiproliferative drug MAM. In our model (Fig. 11), a transient reduction in adolescent neurogenesis (PW3–PW6) may be associated with an impaired hippocampal GABAergic system and subsequently induces PPI deficits in early adulthood. The morphological and behavioral abnormalities in this MAM model were successfully rescued by the application of an EE during a defined vulnerable period.

Postnatal neurogenesis, which is closely related to brain plasticity and adaptability, has received much attention as a target for therapeutics for various neuropsychiatric diseases (Eisch et al., 2008; Kempermann et al., 2008; Thomas and Peterson, 2008; Pieper et al., 2010). There is a reproducible association between a decrease in neurogenesis and impairment in PPI scores in a variety of rodent models (Table 2; Osumi and Guo, 2011). It remains to be shown whether this PPI deficit is temporary or whether it persists into adulthood. Neurogenesis continues to occur throughout life in the hippocampus, but several aspects of neuronal production dramatically change during the postnatal development stage, including an 80% loss of granule cell production from adolescence to young adulthood in rats (He and Crews, 2007). Therefore, it is very likely that neurogenesis during adolescent stages may be more susceptible to the various insults and environmental interventions used in the study of neuropsychiatric disorders.

In the present study, we chose a dose of MAM that was sufficient to block neurogenesis but was low enough to minimize any general physiological disturbance. Although we could not verify a direct effect of MAM on neuronal functions, MAM treatments at perinatal and early postnatal stages have already attracted attention as potential methods for creating animal models of schizophrenia and related mental illness (Flagstad et al., 2004; Penschuck et al., 2006; Lodge et al., 2009; Maekawa et al., 2009). Since our previous MAM treatment in rats from PW4 to PW5 successfully reduces the hippocampal neurogenesis (Maekawa et al., 2009) and such an adolescent period is the stage when the GABAergic system develops in the hippocampus (Kapur and Macdonald, 1999; Fleming et al., 2007), we chose the postnatal stage ~PW4. This simple approach was able to temporarily decrease hippocampal neurogenesis to 74% of the baseline level after the 2 week treatment period, which, as expected, was rescued in early adulthood. Under these conditions, PPI performance was normal at PW6 but was impaired at PW10, suggesting that the delayed PPI deficit was induced by the developmental alteration of postnatal processes, such as abnormal neurogenesis. It remains to be shown whether this PPI deficit is temporary or persists into full adulthood. We further performed experiments to confirm that this PPI deficit persisted into later adulthood at PW18 (Fig. 3*G*). Therefore, adolescent neurogenesis may act in a cell-nonautonomous manner to establish the proper neural circuitry responsible for normal behaviors in adulthood.

A primary finding of our study is the involvement of the GABA interneuron system in the establishment of the PPI-related circuit. Consistent with previous animal studies (Harte et al., 2007; Tseng et al., 2008, Sun et al., 2011), a decrease in the number of GABAergic neurons was observed in our MAM-treated mice. Disturbances in the anatomy, histology, and function of the GABAergic system are implicated in various psychiatric disorders (Charych et al., 2009; Cherlyn et al., 2010; Vinkers et al., 2010). It is known that the $GABA_AR$ agonist benzodiazepines are potentially useful as an adjuvant to neuroleptics in the initial treatment of schizophrenia (Guidotti et al., 2005). However, several side effects, such as amnesia, profound sedation, and development of tolerance, limit their acute or protracted use (Rudolph and Knoflach, 2011). This may be because benzodiazepines have high affinity and intrinsic activity for α1-containing $GABA_ARs$ even after a brief period of treatment, and act indiscriminately as full-positive allosteric modulators at every $GABA_AR$ subtype (Volz et al., 2007). Therefore, to directly implicate the DG GABAergic system in the modulating of sensorimotor gating, we bilaterally infused the muscimol, a potent, selective agonist for the $GABA_ARs$, into the DG region to rescue the PPI deficit in our MAM model. We found that the infusion of muscimol into the DG could ameliorate the PPI deficits in a dose-dependent manner. The MAM-induced PPI deficits were rescued by a lower-dose (10 ng per hemisphere), bilateral acute infusion of muscimol into the DG, but a higher dose (100 ng per hemisphere) failed to rescue the PPI deficits (Fig. 6*E*). It is thus likely that the developmental modification of inhibitory circuits during adolescence may provide susceptibility to the deleterious effects

Table 2. Association of impaired neurogenesis and deficits in prepulse inhibition

Species (strain)	Treatment method	Treatment time	Neurogenesis	Test time point	PPI	References
Lewis rat	Polyinosinic-polycytidylic acid, 4 mg/kg, i.v.	Gestational day 15	Not mentioned	Adult offspring	↓	Cardon M et al., 2010
Sprague Dawley rat	MAM, 25 mg/kg, i.v.	Gestational day 17	Not mentioned	Adult female offspring	↓	Hazane F et al., 2009
Sprague Dawley rat	Ara-c, i.c.v	Adult	~90% decrease at adult stage	4 d after injection	↓	Lau BW et al., 2009
Sprague Dawley rat	Corticosterone, s.c.	Adult	~45% decrease at adult stage	2 weeks after injection	↓	Lau BW et al., 2009
Sprague Dawley rat	Paroxetine, i.p.	Adult	~45% increase at adult stage	2 weeks after injection	Not significant	Lau BW et al., 2009
Sprague Dawley rat	Exercise	Adult	~45% increase at adult stage	2 weeks after injection	Not significant	Lau BW et al., 2009
Sprague Dawley rat	Heterozygous *Pax6* mutant	Not mentioned	~30% and ~40% decrease at 4 weeks and 12 weeks respectively	Not mentioned	Not mentioned	Maekawa M et al., 2005
Sprague Dawley rat	Heterozygous *Pax6* mutant	Not mentioned	Not mentioned	12 weeks	↓	Maekawa M et al., 2009
Sprague Dawley rat	MAM, 10 mg/kg, i.p.	4~5 weeks	~25% decrease at 5 weeks	12 weeks	↓	Maekawa M et al., 2009
129/SvEv C57BL/6	Npas3−/− mice	12 weeks	~85% decrease at 12 weeks	Not mentioned	Not mentioned	Brunskill EW et al., 2005
C57BL/6J mouse	Severe combined immune deficient model	Not mentioned	~20% and ~40% decrease at 4 weeks and 12 weeks respectively	12 weeks	↓	Cardon M et al., 2009
129/SvEv C57BL/6	Npas1−/−:Npas3−/− mice	Not mentioned	Not mentioned	17~20 weeks	↓	Erbel-Sieler C et al., 2004
C57BL/6J mouse	X-irradiated	4 weeks	~90% decrease at 4 weeks	12 weeks	↓	Hayashi H et al., 2008
C57BL/6J mouse	Enrichment environment	3~11 weeks	~65% increase at 12 weeks	12~13 weeks	↑	Iso H et al., 2007
C57BL/6J mouse	Fabp7-null mice	Not mentioned	~30% decrease at 4 weeks	Not mentioned	↓	Watanabe A et al., 2007

of stress or other environmental influences that could trigger pathological changes in a vulnerable circuit. Furthermore, the decreased number of GABAergic neurons was not directly due to the loss of newborn cells directly incorporated into the PPI circuit, as the cells that were generated during PW4–PW6 did not exhibit the morphological features of interneurons (data not shown). Therefore, we propose a scenario in which an initial GABAergic deficit is a developmental consequence mediated by the suppression of neurogenesis during an early stage of development and may result in further deficits in neuronal circuitry and the onset of mental illnesses, such as schizophrenia, during the second or third decades of life.

The beneficial effects of an EE, including increased hippocampal neurogenesis and improved mental and cognitive abilities, have been reported in various paradigms (Schloesser et al., 2010; Bednarczyk et al., 2011) For example, phospholipase C-β1 pathway-deficient mice display impaired hippocampal neurogenesis, spontaneous hyperactivity, and PPI deficits, which are rescued by an EE (McOmish et al., 2008; Manning et al., 2012). An EE is also highly effective at extinguishing submissive behavioral traits that develop under chronic social stress and are critically dependent on adult neurogenesis (Schloesser et al., 2010). In contrast, there are studies that present rather negative results against the behavioral effects of an EE through increasing adult hippocampal neurogenesis (Meshi et al., 2006; Silva et al., 2011). Thus, it is still vague whether the use of an EE has beneficial effects on brain function and behavior (Kempermann et al., 2002; Nithianantharajah and Hannan, 2006; Redolat and Mesa-Gresa, 2012).

The main reason for this conflict is multiple EE paradigms; researchers use different conditions to induce and ameliorate behavioral abnormalities via decreasing and increasing neurogenesis, especially in regard to the age of animals. EE paradigms may exert differential effects on developing and mature brains. There may be critical periods when EE intervention has the greatest impact on specific aspects of brain structure, function, and behavior. In the present study, we first defined a critical period (before PW6) during which the transient decrease in neurogenesis induced by MAM treatment is specifically associated with PPI deficits, anxiety, and hyperactivity at PW10. In this MAM model, the application of EE over this critical period (PW4–PW10) corrected all the three behavioral abnormalities, whereas EE application during PW6–PW10 or PW6–PW12 (data not shown) ameliorated hyperactivity but could not rescue PPI deficits or anxiety. Hence, we propose that the sensitivity and adaptability of EE application to adolescent brains differ from those of the mature brain in terms of the biological vulnerability of neurogenesis and subsequent developmental consequences. This further implicates advantageous gene–environment interactions in the developing human brain and supports early environmental intervention to modulate the late onset of developmental neuropsychiatric diseases.

References

Bast T, Feldon J (2003) Hippocampal modulation of sensorimotor processes. Prog Neurobiol 70:319–345. CrossRef Medline

Bednarczyk MR, Hacker LC, Fortin-Nunez S, Aumont A, Bergeron R, Fernandes KJ (2011) Distinct stages of adult hippocampal neurogenesis are regulated by running and the running environment. Hippocampus 21: 1334–1347. CrossRef Medline

Braff DL, Light GA (2005) The use of neurophysiological endophenotypes to understand the genetic basis of schizophrenia. Dialogues Clin Neurosci 7:125–135. Medline

Braff DL, Geyer MA, Swerdlow NR (2001) Human studies of prepulse inhibition of startle: normal subjects, patient groups, and pharmacological studies. Psychopharmacology (Berl) 156:234–258. CrossRef Medline

Brenes JC, Rodríguez O, Fornaguera J (2008) Differential effect of environment enrichment and social isolation on depressive-like behavior, spontaneous activity and serotonin and norepinephrine concentration in prefrontal cortex and ventral striatum. Pharmacol Biochem Behav 89:85–93. CrossRef Medline

Cadenhead KS, Light GA, Geyer MA, Braff DL (2000) Sensory gating deficits assessed by the P50 event-related potential in subjects with schizotypal personality disorder. Am J Psychiatry 157:55–59. Medline

Cattaneo E, Reinach B, Caputi A, Cattabeni F, Di Luca M (1995) Selective in vitro blockade of neuroepithelial cells proliferation by methylazoxymethanol, a molecule capable of inducing long lasting functional impairments. J Neurosci Res 41:640–647. CrossRef Medline

Charych EI, Liu F, Moss SJ, Brandon NJ (2009) GABA(A) receptors and their associated proteins: implications in the etiology and treatment of

schizophrenia and related disorders. Neuropharmacology 57:481–495. CrossRef Medline

Cherlyn SY, Woon PS, Liu JJ, Ong WY, Tsai GC, Sim K (2010) Genetic association studies of glutamate, GABA and related genes in schizophrenia and bipolar disorder: a decade of advance. Neurosci Biobehav Rev 34:958–977. CrossRef Medline

Ciaroni S, Cuppini R, Cecchini T, Ferri P, Ambrogini P, Cuppini C, Del Grande P (1999) Neurogenesis in the adult rat dentate gyrus is enhanced by vitamin E deficiency. J Comp Neurol 411:495–502. CrossRef Medline

Ciaroni S, Cecchini T, Ferri P, Ambrogini P, Cuppini R, Lombardelli G, Peruzzi G, Del Grande P (2002) Postnatal development of rat dentate gyrus: effects of methylazoxymethanol administration. Mech Ageing Dev 123:499–509. CrossRef Medline

Doischer D, Hosp JA, Yanagawa Y, Obata K, Jonas P, Vida I, Bartos M (2008) Postnatal differentiation of basket cells from slow to fast signaling devices. J Neurosci 28:12956–12968. CrossRef Medline

Douaud G, Mackay C, Andersson J, James S, Quested D, Ray MK, Connell J, Roberts N, Crow TJ, Matthews PM, Smith S, James A (2009) Schizophrenia delays and alters maturation of the brain in adolescence. Brain 132:2437–2448. CrossRef Medline

Eisch AJ, Cameron HA, Encinas JM, Meltzer LA, Ming GL, Overstreet-Wadiche LS (2008) Adult neurogenesis, mental health, and mental illness: hope or hype? J Neurosci 28:11785–11791. CrossRef Medline

Flagstad P, Mørk A, Glenthøj BY, van Beek J, Michael-Titus AT, Didriksen M (2004) Disruption of neurogenesis on gestational day 17 in the rat causes behavioral changes relevant to positive and negative schizophrenia symptoms and alters amphetamine-induced dopamine release in nucleus accumbens. Neuropsychopharmacology 29:2052–2064. CrossRef Medline

Fleming RL, Wilson WA, Swartzwelder HS (2007) Magnitude and ethanol sensitivity of tonic GABAA receptor-mediated inhibition in dentate gyrus changes from adolescence to adulthood. J Neurophysiol 97:3806–3811. CrossRef Medline

Gogtay N, Vyas NS, Testa R, Wood SJ, Pantelis C (2011) Age of onset of schizophrenia: perspectives from structural neuroimaging studies. Schizophr Bull 37:504–513. CrossRef Medline

Guidotti A, Auta J, Davis JM, Dong E, Grayson DR, Veldic M, Zhang X, Costa E (2005) GABAergic dysfunction in schizophrenia: new treatment strategies on the horizon. Psychopharmacology (Berl) 180:191–205. CrossRef Medline

Haddad RK, Rabe A, Dumas R (1972) Comparison of effects of methylazoxymethanol acetate on brain development in different species. Fed Proc 31:1520–1523. Medline

Harte MK, Powell SB, Swerdlow NR, Geyer MA, Reynolds GP (2007) Deficits in parvalbumin and calbindin immunoreactive cells in the hippocampus of isolation reared rats. J Neural Transm 114:893–898. CrossRef Medline

Hayashi F, Takashima N, Murayama A, Inokuchi K (2008) Decreased postnatal neurogenesis in the hippocampus combined with stress experience during adolescence is accompanied by an enhanced incidence of behavioral pathologies in adult mice. Mol Brain 1:22. CrossRef Medline

He J, Crews FT (2007) Neurogenesis decreases during brain maturation from adolescence to adulthood. Pharmacol Biochem Behav 86:327–333. CrossRef Medline

Heckers S, Konradi C (2010) Hippocampal pathology in schizophrenia. Curr Top Behav Neurosci 4:529–553. CrossRef Medline

Hoskison MM, Yanagawa Y, Obata K, Shuttleworth CW (2007) Calcium-dependent NMDA-induced dendric injury and MAP2 loss in acute hippocampal slices. Neuroscience 145:66–79. CrossRef Medline

Hyde TM, Lipska BK, Ali T, Mathew SV, Law AJ, Metitiri OE, Straub RE, Ye T, Colantuoni C, Herman MM, Bigelow LB, Weinberger DR, Kleinman JE (2011) Expression of GABA signaling molecules KCC2, NKCC1, and GAD1 in cortical development and schizophrenia. J Neurosci 31:11088–11095. CrossRef Medline

Kapur J, Macdonald RL (1999) Postnatal development of hippocampal dentate granule cell gamma-aminobutyric acidA receptor pharmacological properties. Mol Pharmacol 55:444–452. Medline

Kempermann G, Kuhn HG, Gage FH (1997) More hippocampal neurons in adult mice living in an enriched environment. Nature 386:493–495. CrossRef Medline

Kempermann G, Gast D, Gage FH (2002) Neuroplasticity in old age: sustained fivefold induction of hippocampal neurogenesis by long-term environmental enrichment. Ann Neurol 52:135–143. CrossRef Medline

Kempermann G, Krebs J, Fabel K (2008) The contribution of failing adult hippocampal neurogenesis to psychiatric disorders. Curr Opin Psychiatry 21:290–295. CrossRef Medline

Lewis DA (1997) Development of the prefrontal cortex during adolescence: insights into vulnerable neural circuits in schizophrenia. Neuropsychopharmacology 16:385–398. CrossRef Medline

Lewis DA, Levitt P (2002) Schizophrenia as a disorder of neurodevelopment. Annu Rev Neurosci 25:409–432. CrossRef Medline

Lewis DA, Cruz D, Eggan S, Erickson S (2004) Postnatal development of prefrontal inhibitory circuits and the pathophysiology of cognitive dysfunction in schizophrenia. Ann N Y Acad Sci 1021:64–76. CrossRef Medline

Lodge DJ, Behrens MM, Grace AA (2009) A loss of parvalbumin-containing interneurons is associated with diminished oscillatory activity in an animal model of schizophrenia. J Neurosci 29:2344–2354. CrossRef Medline

Louchart-de la Chapelle S, Nkam I, Houy E, Belmont A, Ménard JF, Roussignol AC, Siwek O, Mezerai M, Guillermou M, Fouldrin G, Levillain D, Dollfus S, Campion D, Thibaut F (2005) A concordance study of three electrophysiological measures in schizophrenia. Am J Psychiatry 162:466–474. CrossRef Medline

Maekawa M, Takashima N, Matsumata M, Ikegami S, Kontani M, Hara Y, Kawashima H, Owada Y, Kiso Y, Yoshikawa T, Inokuchi K, Osumi N (2009) Arachidonic acid drives postnatal neurogenesis and elicits a beneficial effect on prepulse inhibition, a biological trait of psychiatric illnesses. PLoS One 4:e5085. CrossRef Medline

Manning EE, Ransome MI, Burrows EL, Hannan AJ (2012) Increased adult hippocampal neurogenesis and abnormal migration of adult-born granule neurons is associated with hippocampal-specific cognitive deficits in phospholipase C-β1 knockout mice. Hippocampus 22:309–319. CrossRef Medline

Matsumata M, Sakayori N, Maekawa M, Owada Y, Yoshikawa T, Osumi N (2012) The effects of Fabp7 and Fabp5 on postnatal hippocampal neurogenesis in the mouse. Stem Cells 30:1532–1543. CrossRef Medline

McOmish CE, Burrows E, Howard M, Scarr E, Kim D, Shin HS, Dean B, van den Buuse M, Hannan AJ (2008) Phospholipase C-beta1 knockout mice exhibit endophenotypes modeling schizophrenia which are rescued by environmental enrichment and clozapine administration. Mol Psychiatry 13:661–672. CrossRef Medline

Meshi D, Drew MR, Saxe M, Ansorge MS, David D, Santarelli L, Malapani C, Moore H, Hen R (2006) Hippocampal neurogenesis is not required for behavioral effects of environmental enrichment. Nat Neurosci 9:729–731. CrossRef Medline

Nithianantharajah J, Hannan AJ (2006) Enriched environments, experience-dependent plasticity and disorders of the nervous system. Nat Rev Neurosci 7:697–709. CrossRef Medline

Osumi N, Guo N (2011) Impaired neuroscience as a risk factor for schizophrenia and related mental diseases. In: Neurogenesis in the Adult Brain II (Seki T, Sawamoto K, Parent JM, Alvarez-Buylla A, eds), pp 109–131. Tokyo: Springer.

Penschuck S, Flagstad P, Didriksen M, Leist M, Michael-Titus AT (2006) Decrease in parvalbumin-expressing neurons in the hippocampus and increased phencyclidine-induced locomotor activity in the rat methylazoxymethanol (MAM) model of schizophrenia. Eur J Neurosci 23:279–284. CrossRef Medline

Pieper AA, Xie S, Capota E, Estill SJ, Zhong J, Long JM, Becker GL, Huntington P, Goldman SE, Shen CH, Capota M, Britt JK, Kotti T, Ure K, Brat DJ, Williams NS, MacMillan KS, Naidoo J, Melito L, Hsieh J et al. (2010) Discovery of a proneurogenic, neuroprotective chemical. Cell 142:39–51. CrossRef Medline

Plümpe T, Ehninger D, Steiner B, Klempin F, Jessberger S, Brandt M, Römer B, Rodriguez GR, Kronenberg G, Kempermann G (2006) Variability of doublecortin-associated dendrite maturation in adult hippocampal neurogenesis is independent of the regulation of precursor cell proliferation. BMC Neurosci 7:77. CrossRef Medline

Rapoport JL, Addington AM, Frangou S, Psych MR (2005) The neurodevelopmental model of schizophrenia: update 2005. Mol Psychiatry 10:434–449. CrossRef Medline

Redolat R, Mesa-Gresa P (2012) Potential benefits and limitations of enriched environments and cognitive activity on age-related behavioural decline. Curr Top Behav Neurosci 10:293–316. CrossRef Medline

Rudolph U, Knoflach F (2011) Beyond classical benzodiazepines: novel

therapeutic potential of GABAA receptor subtypes. Nat Rev Drug Discov 10:685–697. CrossRef Medline

Saint Marie RL, Miller EJ, Breier MR, Weber M, Swerdlow NR (2010) Projections from ventral hippocampus to medial prefrontal cortex but not nucleus accumbens remain functional after fornix lesions in rats. Neuroscience 168:498–504. CrossRef Medline

Schloesser RJ, Lehmann M, Martinowich K, Manji HK, Herkenham M (2010) Environmental enrichment requires adult neurogenesis to facilitate the recovery from psychosocial stress. Mol Psychiatry 15:1152–1163. CrossRef Medline

Silva CF, Duarte FS, Lima TC, de Oliveira CL (2011) Effects of social isolation and enriched environment on behavior of adult Swiss mice do not require hippocampal neurogenesis. Behav Brain Res 225:85–90. CrossRef Medline

Sisk CL, Zehr JL (2005) Pubertal hormones organize the adolescent brain and behavior. Front Neuroendocrinol 26:163–174. CrossRef Medline

Spear LP (2000) The adolescent brain and age-related behavioral manifestations. Neurosci Biobehav Rev 24:417–463. CrossRef Medline

Sun Y, Farzan F, Barr MS, Kirihara K, Fitzgerald PB, Light GA, Daskalakis ZJ (2011) Gamma oscillations in schizophrenia: mechanisms and clinical significance. Brain Res 1413:98–114. CrossRef Medline

Swerdlow NR, Geyer MA (1998) Using an animal model of deficient sensorimotor gating to study the pathophysiology and new treatments of schizophrenia. Schizophr Bull 24:285–301. CrossRef Medline

Swerdlow NR, Weber M, Qu Y, Light GA, Braff DL (2008) Realistic expectations of prepulse inhibition in translational models for schizophrenia research. Psychopharmacology (Berl) 199:331–388. CrossRef Medline

Tamamaki N, Yanagawa Y, Tomioka R, Miyazaki J, Obata K, Kaneko T (2003) Green fluorescent protein expression and colocalization with calretinin, parvalbumin, and somatostatin in the GAD67-GFP knock-in mouse. J Comp Neurol 467:60–79. CrossRef Medline

Tamminga CA, Stan AD, Wagner AD (2010) The hippocampal formation in schizophrenia. Am J Psychiatry 167:1178–1193. CrossRef Medline

Thomas RM, Peterson DA (2008) Even neural stem cells get the blues: evidence for a molecular link between modulation of adult neurogenesis and depression. Gene Expr 14:183–193. Medline

Tseng KY, Lewis BL, Hashimoto T, Sesack SR, Kloc M, Lewis DA, O'Donnell P (2008) A neonatal ventral hippocampal lesion causes functional deficits in adult prefrontal cortical interneurons. J Neurosci 28:12691–12699. CrossRef Medline

Vinkers CH, Mirza NR, Olivier B, Kahn RS (2010) The inhibitory GABA system as a therapeutic target for cognitive symptoms in schizophrenia: investigational agents in the pipeline. Expert Opin Investig Drugs 19:1217–1233. CrossRef Medline

Volz A, Khorsand V, Gillies D, Leucht S (2007) Benzodiazepines for schizophrenia. Cochrane Database Syst Rev 1:CD006391. Medline

Weinberger DR (1996) On the plausibility of "the neurodevelopmental hypothesis" of schizophrenia. Neuropsychopharmacology 14:1S–11S. CrossRef Medline

Japanese Journal of Applied Physics 52 (2013) 07HF21 **REGULAR PAPER**
http://dx.doi.org/10.7567/JJAP.52.07HF21

Ultrasonic Measurement of Microdisplacement Induced by Acoustic Radiation Force

Ryo Nagaoka[1]*, Takuya Izumi[1], Yosuke Komatsu[1], Kazuto Kobayashi[2], and Yoshifumi Saijo[1]

[1]*Graduate School of Biomedical Engineering, Tohoku University, Sendai 980-8579, Japan*
[2]*Division of Research and Development, Honda Electronics Co., Ltd., Toyohashi, Aichi 411-3193, Japan*

Received November 23, 2012; accepted January 30, 2013; published online July 22, 2013

Quantitative evaluation of human skin aging is achieved by measuring the viscoelasticity of the skin. In the present study, microdisplacement induced by acoustic radiation force (ARF) is quantitatively measured by high-frequency ultrasonography (HFUS) and the result is confirmed by laser-Doppler velocimetry (LDV). Poly(vinyl alcohol) (PVA) with 1% cellulose particles was used as the biological phantom. A concave piezoelectric zirconate titanate (PZT) transducer with a diameter and focal length of 3 cm was used as an applicator to generate ARF. Microdisplacement at each depth of PVA was measured by the phased tracking method at 100 MHz of ultrasound with a repetition rate of 2000 Hz. When 80 tone-burst pulses were applied, the displacement measured by HFUS was 9 μm and the same result was obtained by LDV. As the displacement at each depth of PVA is measurable using ARF and the HFUS system, the system could be applied to measuring the viscoelasticity of the layered structure of the human skin. © 2013 The Japan Society of Applied Physics

1. Introduction

In aging societies, many people are interested in skin aging. They hope to deal with aging and maturity correctly. Wrinkled skin and sagging skin are closely related to both the quantity and quality of collagen inside the dermis. With the change in quantity and quality of collagen, flexibility and retractility change. It is considered that the viscoelasticity of the human skin is linked to the collagen and microstructures within the dermis, but the viscoelasticity of the human skin has not been reported well. The microstructures of the human skin are the sebaceous glands, hair follicles, and capillary blood vessels. The microstructures of the human skin were observed by ultrasound microscopy at a central frequency of 100 MHz.[1)] In our present study, the epidermis and dermis were observed distinctively. The hair follicles were reported as hypoechoic and the dermis as echo-rich. Also, the human skin was observed using a 20 MHz spherically focused single-element transducer,[2)] and the elasticity of the skin was assessed by applying suction to the skin surface with a stepwise increase in vacuum.[3)] In the latter, the nevus inside the dermis was observed by strain imaging. In our previous study,[4)] the human skin structures, especially the sebaceous glands deep in dermis, was observed by three-dimensional ultrasound microscopy at a central frequency of 120 MHz. The sebaceous glands also act as a cushion of the skin in addition to their classical role of secreting sebum and some hormones.

High-resolution ultrasonic measurement is available by high-frequency ultrasonography (HFUS) because the resolution is proportional to ultrasonic wavelength, which is inversely proportional to ultrasonic frequency. 20-μm resolution is acquired at 100 MHz. It is now nearly possible to observe the human skin structures and function in vivo. The depth from the surface of the human skin to the bottom of the dermis is almost equal to the depth of penetration of HFUS. HFUS is suitable for in vivo measurement of the human skin and provides information on morphology and mechanical properties.

In the late 1980s, viscoelasticity, which is a key parameter in the diagnosis of cancer and fibrosis has been researched by ultrasonography by Krouskop et al.,[5)] Yamakosi et al.,[6)] and Ophir et al.[7)] Research over the past two decades has brought about drastic developments in the measurement of elasticity with higher accuracy. However, in this method, human tissues need to be pushed at an adequate pressure to generate deformation. This is difficult to do so and the result depends on the degree of proficiency of operators. Acoustic radiation force impulse (ARFI) imaging[8–16)] is a new imaging modality, by which tissue viscoelasticity is evaluated by measurement of shear wave or displacement induced by acoustic radiation force. This method enables the evaluation of the mechanical properties of human tissue by measuring the velocity of shear wave and to press uniformly the region of interest regardless of the proficiency of operators or patients. The clinical viability of a method of acoustic remote palpation is widely investigated in vivo. Acoustic radiation force (ARF) has been used to generate internal mechanical excitation noninvasively. With measurement of the displacement generated by the internal mechanical excitation, ARFI imaging is capable of imaging local variations in the mechanical properties of soft tissue.

Our goal is the development of a hybrid measurement method with HFUS and ARFI imaging to reveal the origin of skin viscoelasticity. In this study, the objectives are to generate the microdisplacement of poly(vinyl alcohol) (PVA) by ARF with our original applicator and compare this result of high-frequency ultrasonic measurement with that of laser-Dopper velocimetry.

2. Experimental Methods

2.1 ARF

ARF[17)] is a phenomenon associated with the propagation of acoustic waves through a dissipative medium and the time-averaged force exerted by an acoustic field on an object. This force is an example of universal phenomenon in any wave motion that introduces some type of a unidirectional force on absorbing or reflecting targets in the wave path. Radiation force is produced by a change in the energy density of an incident acoustic field. The acoustic radiation pressure P_R has two components in the beam direction and another transverse to the beam direction:[18,19)]

$$\boldsymbol{P}_R(t) = \boldsymbol{d}_r e(t), \tag{1}$$

where $\boldsymbol{d}_r$ is the drag coefficient with two components, and $e(t)$ is the energy density of incident ultrasonic pressure field $p(t)$. Physically, $\boldsymbol{d}_r$ represents the scattering and absorbing properties of the object and is given by

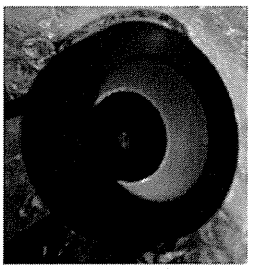

(a)

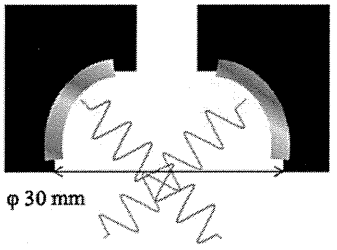

(b)

Fig. 1. (Color online) Applicator of ARF: (a) image and (b) diagram.

$$d_r = pS^{-1}\left(\Pi_a + \Pi_s - \int \gamma \cos\alpha_s \, dS\right) + qS^{-1}\int \gamma \sin\alpha_s \, dS, \quad (2)$$

where $\boldsymbol{p}$ and $\boldsymbol{q}$ are the unit vectors in the beam direction and normal to it, respectively. The quantities Π_a and Π_s are the total absorbed and scattered powers, respectively, and γ is the scattered intensity. α_s is the angle between the incident acoustic field and the scattered intensity, and dS is the area element.

A hemispherical PZT transducer with a central frequency of 1 MHz and an aperture diameter of 30 mm is used as the applicator of ARF instead of a focused acoustic beam. The focal length is 15 mm. Figure 1(a) shows the applicator of acoustic radiation force. The input to the applicator is tone-burst pulses at intervals of 1 ms (Fig. 2). From the simplified model of our applicator [Fig. 1(b)], incident ultrasonic pressure field $p(x,t)$ is obtained by

$$p(x,t) = P_0 \cos kx \cdot \cos(\omega t - \varphi), \quad (3)$$

where P_0 is the amplitude of incident ultrasonic pressure, k is the wave number of incident ultrasonic pressure, ω is the angular frequency, and φ is the phase lag. The sound distribution of our applicator was measured using acoustic intensity measurement system (AIMS) 3 (Fig. 3), which is a hydrophone scanning system and enhances the productivity

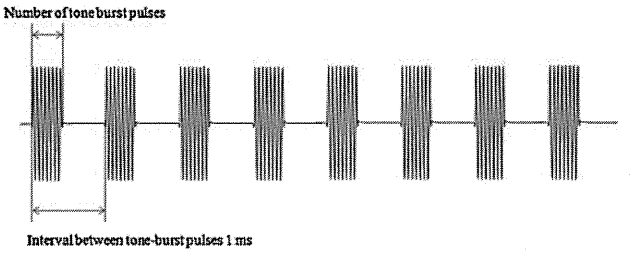

Fig. 2. (Color online) Tone-burst pulses.

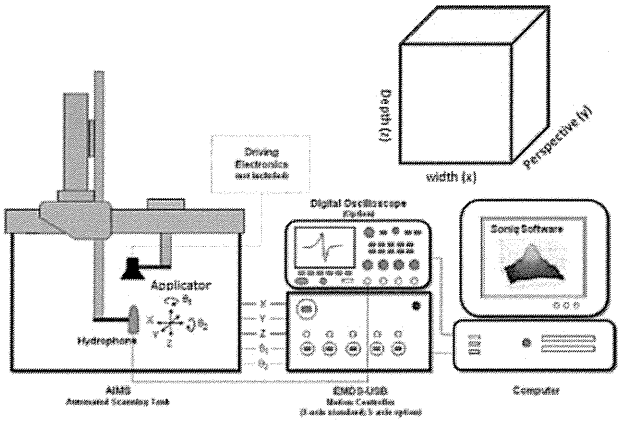

Fig. 3. (Color online) AIMS system.

of acoustic instrumentation to map acoustic field in solution. The hydrophone is a needle-type MH28-6, thin-film poly-(vinylidene difluoride) (PVDF) with a 0.5–20 MHz bandwidth. The measurement conditions are as follows: the input signal to the applicator is tone-burst pulses at intervals of 1 ms, and the measurement position is the focus of the applicator. Figure 4 shows the sound pressure changes at the focal position at each pulse length. While considering the response of the applicator, the pressure field is amplitude-modulated, as shown in Fig. 4, and can be approximated by

$$p_r(x,t) = P_0 \cos kx \cdot \cos(\omega t - \varphi) \cdot \cos\left(\frac{2\pi t}{4T_p}\right), \quad (4)$$

where T_p is the cycle time of the envelop of input tone-burst pulses, which should be computed by the number of tone-burst pulses. The energy density $e(x,t)$ is given by

$$e(x,t) = \frac{\langle (p_r(x,t))^2 \rangle}{\rho c^2} = \frac{P_0^2}{4\rho c^2}\cos^2 kx \cdot \left[1 + \cos\left(\frac{2\pi t}{4T_p}\right)\right], \quad (5)$$

where ρ and c are the density and propagation speed in the medium, respectively. Hence, the acoustic radiation pressure is given by

$$P_R(x,t) = d_r e(x,t) = \left[pS^{-1}\left(\Pi_a + \Pi_s - \int \gamma \cos\alpha_s \, dS\right) + qS^{-1}\int \gamma \sin\alpha_s \, dS\right]. \frac{P_0^2}{4\rho c^2}\cos^2 kx \cdot \left[1 + \cos\left(\frac{2\pi t}{4T_p}\right)\right]. \quad (6)$$

The reflection coefficient R is defined by

$$R = \frac{Z_{object} - Z_{water}}{Z_{object} + Z_{water}} = \frac{\rho_O c_O - \rho_W c_W}{\rho_O c_O + \rho_W c_W}. \quad (7)$$

The density ρ_W and sound speed c_W of water are assumed as 1.0×10^3 kg/m^3 and 1500 m/s, respectively. The density ρ_O and sound speed c_O are the parameters of human tissues. The density ρ_O of human tissues is considered to be nearly close

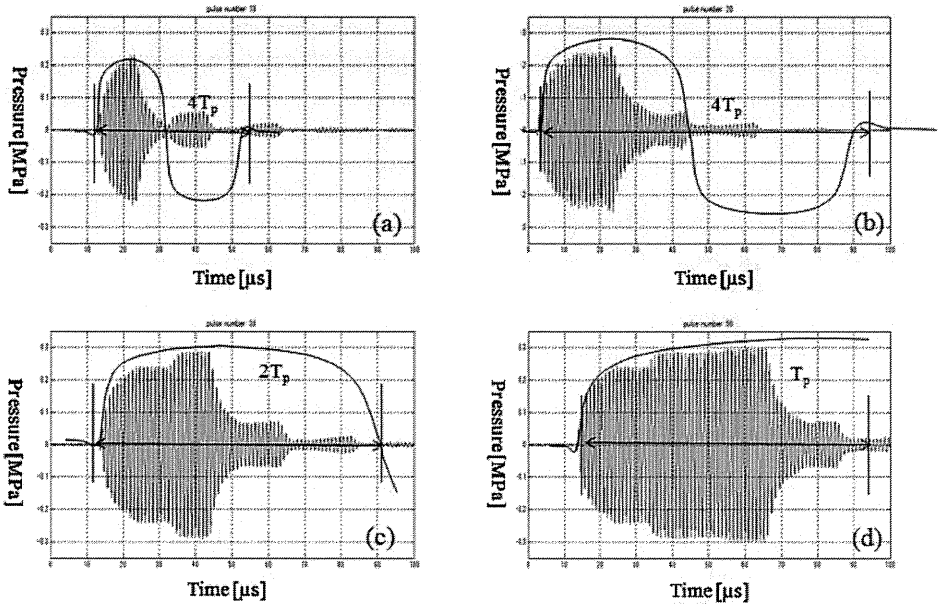

Fig. 4. (Color online) Sound distribution of applicator: numbers of pulses (a) 10 (b) 20 (c) 30, and (d) 50.

to that of water, i.e., $1.0 \times 10^3\,\mathrm{kg/m^3}$. The sound speed c_0 of the skin is from 1450–1510 m/s.[20] The reflection coefficient R is 0.034. Hence, the reflection energy R^2 is almost zero, or the scattered energy Π_s is also considered to be zero. The scattered intensity γ is also small. The attenuations of the human skin α_{skin} are reported to be in the range from 2.1 to 9.2 dB/cm in conventional US. The thickness from the epidermis to the dermis is about 2 mm. The lowest attenuation by the human skin is from 1.00097 to 1.00425% against the attenuation of water. The influence of attenuation is greatest.

2.2 PVA

PVA cryogels are polymers. PVA has been commonly used for building biological tissue-mimicking phantoms.[21–24] The physical properties of PVA depend on dehydration during heating at the first step of preparation, the speed of decreasing and increasing temperature, the minimum temperature at which the volume of the sample was reached, and the number of freeze-thaw cycles. PVA powder was dissolved in a mixture of dimethyl sulfoxide (DMSO) aqueous solution (80 wt%). Cellulose particles are added into this solution (φ38 μm, 1 wt%). The particles are employed as acoustic scatterers. The PVA powder in the mixture solution was stirred for 2 h at 373.15 K until dissolution, and then the solution was poured into an acrylic plastic mold with dimensions of $15 \times 7.5 \times 4\,\mathrm{cm^3}$ up to a height of 1 cm. The mold was maintained at 253.15 K for 24 h to promote gelation of the PVA solution.

2.3 PVA in LDV

The principle of LDV is based on the heterodyne interferometric method; while superposing two waves that are slightly different in frequency, the difference in frequency, called the "surge" or "beat", can be observed. Needed information is extracted from the observed surge. The

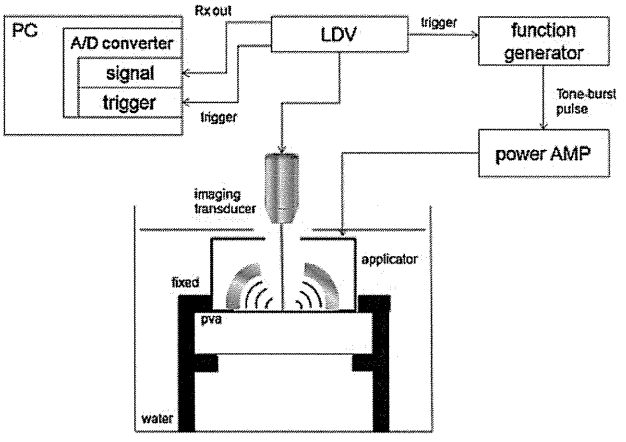

Fig. 5. (Color online) LDV system.

velocity on the PVA surface induced by acoustic radiation force is measured by LDV under two conditions. Figure 5 shows the measurement system. One condition is changing the input voltage to 15, 20, 25, 30, and 35 V with the duration of a tone-burst pulse set at 30 μs. Another is changing the number of tone-burst pulses at 5, 10, 20, 30, 50, and 80 μs with the input voltage set at 20 V. Displacement, duration time, and center frequency of surface oscillations are measured under these conditions. The displacement can be obtained by integration over time.

2.4 PVA in HFUS measurement

In accordance with the result of LDV, input voltage and the duration of tone-burst pulses are determined. The center frequency of oscillations of PVA surface is the most important factor for decision. An electric impulse was generated using a high-speed switching semiconductor. The starting pulse was within 400 ps, the pulse width was 2 ns, and the pulse

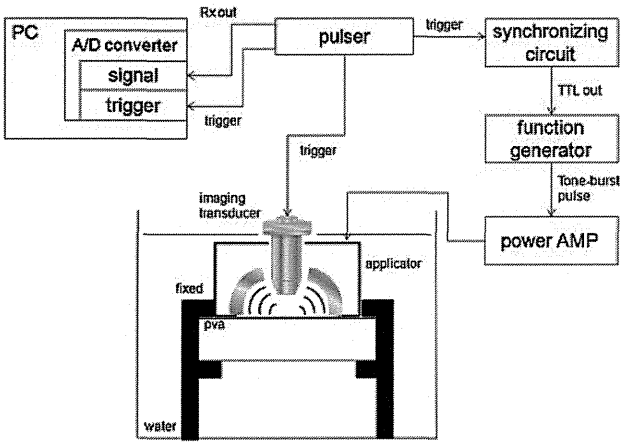

Fig. 6. (Color online) HFUS system.

voltage was 40 V. The frequency range of the impulses was approximately up to 500 MHz. The electric pulse was used to excite a vinylidene fluoride and trifluoroethylene P(VDF–TrFE) transducer. The aperture diameter of the transducer was 2 mm, and the focal length was 4 mm. The central frequency was 100 MHz, the bandwidth (−6 dB) was in the range of 50–150 MHz, and the pulse repetition rate was 2000 Hz. The pulse was synchronized with a 100 MHz ultrasound at 2000 Hz repetition rate. With the position of the transducer fixed, the reflections from PVA were received by the transducer and were introduced into a Windows-based personal computer (PC; Pentium 4, 3.40 GHz, 1 GB RAM, and 250 GB HDD) with a high-speed digitizer card (Acqiris DP 1400, Geneva, Switzerland). The frequency was 500 MHz, and the maximum sampling rate was 2 GS/s. Figure 6 shows the HFUS system.

2.5 Phased-tracking method

The microdisplacement generated by acoustic radiation force needs to be estimated accurately to image local variations in the mechanical properties of soft tissue. The phased-tracking method was proposed to measure the small changes in thickness of the arterial wall due to the heartbeat.[25,26] The standard cross-correlation method enables only the estimation of discrete velocity or displacement. However, the phased-tracking method enables the continuous estimation of velocity or displacement. This is because in the latter method, the phase difference between the reference signal and the object signal is employed for the estimation of algorithm. These signals are reflected RF signals with the angular frequency $\omega_0 = 2\pi f_0$ on the object, transmitted at a time interval of ΔT from the ultrasonic transducer. For phased-tracking method, the average velocity is given by

$$v\left(z, t+\frac{\Delta T}{2}\right) = c \cdot \frac{\Delta\theta(z,t)}{2\omega_0 \Delta T}, \tag{8}$$

where z is the depth of the object at a time t and $\Delta\theta$ is the phase difference. By manually setting up the first position of the object, the next position of the object after a time interval of ΔT is obtained by

$$x(t) = x(t-\Delta T) + v\left(z, t+\frac{\Delta T}{2}\right) \cdot \Delta T. \tag{9}$$

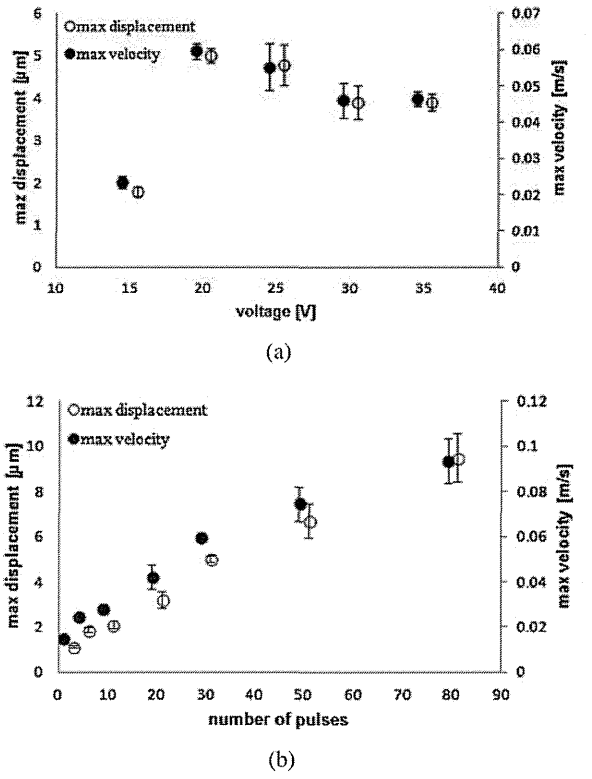

Fig. 7. Results of LDV: displacement and velocity (a) voltage; (b) number of pulses.

3. Results

3.1 Results of measurement by LDV

A displacement generated by ARF is calculated by integrating a measured velocity curve. Figure 7(a) shows velocity and displacement at various input voltages. In Fig. 7(a), both velocity and displacement increase from 15 to 20 V, and gradually decrease from 20 to 35 V. Figure 7(b) shows velocity and displacement at various numbers of tone-burst pulses. In the entire range, linear relationships between velocity and voltage and also between displacement and voltage are shown.

Figure 8(a) shows the duration of oscillations of the PVA surface. Rising time is defined as the start of a hundredth of maximum velocity and fall time is defined as the end of a hundredth of maximum velocity. Duration is defined as the difference between fall time and rising time. Figure 9 shows oscillations of the PVA surface. The duration oscillations linearly increased with increasing number of tone-burst pulses. Figure 8(b) shows the center frequency of oscillations of the PVA surface.

3.2 Results of measurement by HFUS

According to the results of LDV, the input voltage was set at 20 V and the duration of tone-burst pulses at 80 μs. RF signals are transmitted from the imaging transducer with a central frequency of 100 MHz, and the reflected signals from the surface of PVA are acquired by an analog-to-digital (A/D) digitizer. M-mode images are constructed from the acquired signals. The spatial distribution of displacements inside the phantom can be estimated from the M-

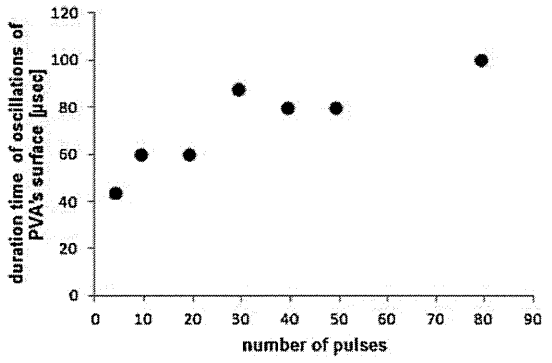

(a)

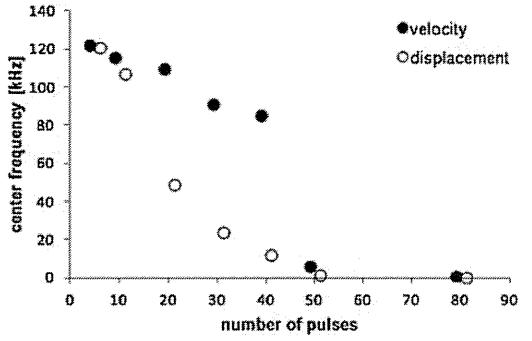

(b)

Fig. 8. Results of LDV: (a) duration; (b) center frequency.

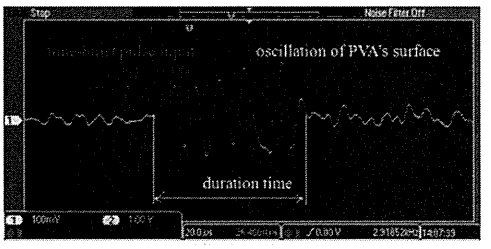

Fig. 9. (Color online) Oscillations of PVA surface (30 tone-burst pulses).

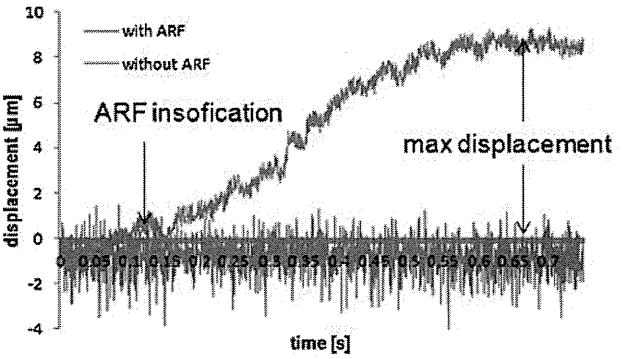

(a)

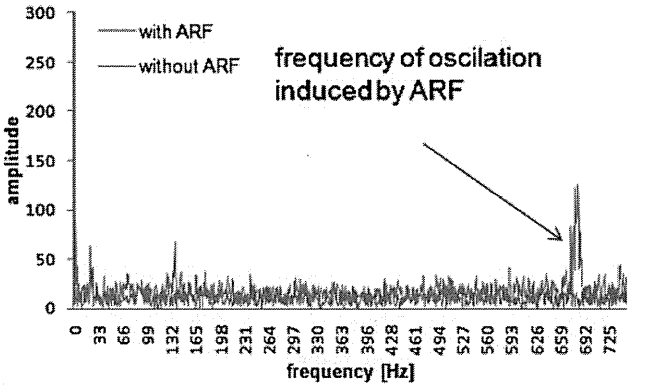

(b)

Fig. 10. (Color online) Results of HFUS: (a) displacement; (b) center frequency.

mode images. The displacement at the surface of the object induced by ARF was measured by the phased-tracking method. The tracking line was assigned to only the surface of PVA to compare the results with those of LDV measurements. The estimated displacement is shown in Fig. 10(a), and the maximum amplitude of the measured displacement was 9 μm. Figure 10(b) shows the frequency of displacement. The calculated error mean square between the measurements by the two methods was 0.553 μm. This value indicates that the result was confirmed by LDV.

4. Discussion

4.1 Results of measurement by LDV

In Fig. 7(a), the measurement in the range from 20 to 35 V shows no linear relationship. There are two possible reasons for this: One is the standing wave generated by the interference between an incident wave and a reflected wave. The other one is acousto-optics modulation, that is, a light is modulated by an intense ultrasound. The effects of this modulation need to be examined.

There is a difference between the center frequency of velocity and displacement in Fig. 8(b). This is because of the calculation of displacement from integrating velocity. This integral plays a role as a low-pass filter and the high frequency of velocity would be cut off.

In Fig. 8(b) the frequency inversely decreased with increasing number of tone-burst pulses. It is considered that the frequency is dependent on the time width of tone-burst pulses. The time term of Eq. (10) is expressed by

$$P_{\mathrm{R}}(x,t) = pS^{-1}\left(\Pi_{\mathrm{a}} + \Pi_{\mathrm{s}} - \int \gamma \cos\alpha_{\mathrm{s}}\, dS\right) \times \left[1 + \cos\left(\frac{2\pi t}{4T_{\mathrm{p}}}\right)\right]. \quad (10)$$

The frequency of oscillations f_{object} is given by

$$f_{\mathrm{object}} = \frac{1}{4T_{\mathrm{p}}}. \quad (11)$$

From Eq. (10), the frequency is inversely proportional to four times as much as T_{p}. The measured result showed a similar trend to result calculated using Eq. (10), but there was slight disparity between experimental value and the value calculated using the theoretical equation, which is attributed to the longer oscillation duration of the applicator generated by not-perfect electromechanical coupling. For example, in the case of 100 μs tone-burst pulse inputs to the applicator, the oscillation duration is more than 100 μs, not 100 μs.

4.2 Results of measurement by HFUS

In Fig. 10(a), the estimated displacement asymptotically responded to the external force ARF, which was similar to that displacement measured by LDV. Additionally, this displacement actuated by ARF resembles a step response of tissue in the Voigt model.[27,28] It is possible that the viscoelasticity of an object can be estimated by fitting measurement displacement to this tissue model. The frequency of the oscillation induced by ARF was approximately the same as that in DC ranging from 660 to 720 Hz [Fig. 10(b)]. This frequency range was possible in the presence of ARF, but not in the absence of ARF. The DC component arises from the DC term of Eq. (10) and the higher frequency range arises from the AC component of Eq. (10).

5. Conclusions

The velocity of oscillation of the PVA surface was measured at various input voltages and durations. Displacement was obtained by integrating measured velocity. According to the result of LDV, microdisplacement was measured by HFUS. The results of the two methods were compared, and the measured displacements were almost equivalent. This study showed a relationship between the oscillations of the PVA surface and the parameters of tone-burst pulses, indicating the availability of our original applicator. As further research, we will estimate the human skin viscoelasticity using the measured displacement and the tissue Voigt model, and HFUS with ARF may be applied to human skin viscoelasticity measurement. Such a study will reveal the origin of human skin viscoelasticity.

Acknowledgments

We acknowledge the Grants-in-Aid for Scientific Research B (22300175), and Challenging Exploratory Research (23650300) from the Japan Society for the Promotion of Science, Technology and Regional Innovation Program from the Ministry of Economy, Trade and Industry.

1) S. E. Gammal, C. E. Gammal, K. Kaspar, C. Pieck, P. Altmeyer, M. Vogt, and H. Ermert: J. Invest. Dermatol. **113** (1999) 821.
2) M. Vogt and H. Ermert: IEEE Trans. Ultrason. Ferroelectr. Freq. Control **55** (2008) 1975.
3) M. Vogt and H. Ermert: IEEE Trans. Ultrason. Ferroelectr. Freq. Control **52** (2005) 375.
4) K. Kumagai, H. Koike, Y. Kudo, R. Nagaoka, K. Kubo, K. Kobayashi, and Y. Saijo: Conf. Proc. 33rd IEEE EMBC, 2011, p. 7199.
5) T. A. Krouskop, D. R. Doughtery, and S. F. Levinson: J. Rehabil. Res. Dev. **24** (1987) 1.
6) Y. Yamakoshi, J. Sato, and T. Sato: IEEE Trans. Ultrason. Ferroelectr. Freq. Control **37** (1990) 45.
7) J. Ophir, I. Céspedes, H. Ponnekanti, Y. Yazdi, and X. Li: Ultrason. Imaging **13** (1991) 111.
8) K. Nightingale, M. S. Soo, R. Nightingale, and G. Trahey: Ultrasound Med. Biol. **28** (2002) 227.
9) K. Nightingale, S. McAleavey, and G. E. Trahey: Ultrasound Med. Biol. **29** (2003) 1715.
10) J. Bercoff, M. Tanter, and M. Fink: IEEE Trans. Ultrason. Ferroelectr. Freq. Control **51** (2004) 396.
11) S. Chen, M. Fatemi, and J. F. Greenleaf: J. Acoust. Soc. Am. **112** (2002) 884.
12) S. Chen, M. Fatemi, and J. F. Greenleaf: J. Acoust. Soc. Am. **115** (2004) 2781.
13) H. Hasegawa, M. Takahashi, Y. Nishio, and H. Kanai: Jpn. J. Appl. Phys. **45** (2006) 4706.
14) J. Yamaguchi, H. Hasegawa, and H. Kanai: J. Med. Ultrason. **39** (2012) 279.
15) T. Miwa, R. Kumar Parajuli, R. Tomizawa, and Y. Yamakoshi: Jpn. J. Appl. Phys. **50** (2011) 07HF07.
16) T. Miwa, Y. Yoshihara, K. Kanazawa, R. Kumar Parajuli, and Y. Yamakoshi: Jpn. J. Appl. Phys. **51** (2012) 07GF13.
17) G. R. Torr: Am. J. Phys. **52** (1984) 402.
18) M. Fatemi and J. F. Greenleaf: Proc. Natl. Acad. Sci. U.S.A. **96** (1999) 6603.
19) M. Fatemi, L. E. Wold, A. Alizad, and J. F. Greenleaf: IEEE Trans. Med. Imaging **21** (2002) 1.
20) S. A. Goss, R. L. Johnston, and F. Dunn: J. Acoust. Soc. Am. **64** (1978) 423.
21) H. Kosukegawa, K. Mamada, K. Kuroki, L. Liu, K. Inoue, T. Hayase, and M. Ohta: J. Fluid Sci. Technol. **3** (2008) 533.
22) J. Fromageau, J. L. Gennisson, C. Schmitt, R. L. Maurice, R. Mongrain, and G. Cloutier: IEEE Trans. Ultrason. Ferroelectr. Freq. Control **54** (2007) 498.
23) C. Jia, K. Kim, W. F. Weitzel, C. Jia, J. M. Rubin, and T. J. Kolias: Proc. IEEE Ultrasonics Symp., 2006, p. 1317.
24) B. Lesniak-Plewinska, S. Cygan, K. Kaluzynski, J. D'hooge, J. Zmigrodzki, E. Kowalik, M. Kordybach, and M. Kowalski: Ultrasound Med. Biol. **36** (2010) 1145.
25) H. Kanai, M. Sato, Y. Koiwa, and N. Chubachi: IEEE Trans. Ultrason. Ferroelectr. Freq. Control **43** (1996) 791.
26) H. Hasegawa and H. Kanai: IEEE Trans. Ultrason. Ferroelectr. Freq. Control **53** (2006) 2050.
27) W. F. Walker, F. J. Fernandez, and L. A. Negron: Phys. Med. Biol. **45** (2000) 1437.
28) A. Gautieri, S. Vesentini, A. Redaelli, and M. J. Buehler: Matrix Biol. **31** (2012) 141.

Journal of Controlled Release 172 (2013) 879–884

Contents lists available at ScienceDirect

Journal of Controlled Release

journal homepage: www.elsevier.com/locate/jconrel

NANOMEDICINE

Photothermal therapy of tumors in lymph nodes using gold nanorods and near-infrared laser light

Tatsuki Okuno [a], Shigeki Kato [a], Yuriko Hatakeyama [a], Junnosuke Okajima [b], Shigenao Maruyama [b], Maya Sakamoto [c], Shiro Mori [d], Tetsuya Kodama [a,*]

[a] Laboratory of Biomedical Engineering for Cancer, Department of Biomedical Engineering, Graduate School of Biomedical Engineering, Tohoku University, 4-1 Seiryo, Aoba, Sendai, Miyagi 980-8575, Japan
[b] Institute of Fluid Science, Tohoku University, 2-1-1 Katahira, Aoba Ward, Sendai, Miyagi 980-8577, Japan
[c] Department of Oral Diagnosis, Tohoku University Hospital, 1-1 Seiryo, Aoba Ward, Sendai, Miyagi 980-8575, Japan
[d] Department of Oral and Maxillofacial Surgery, Tohoku University Hospital, 1-1 Seiryo, Aoba Ward, Sendai, Miyagi 980-8575, Japan

ARTICLE INFO

Article history:
Received 13 August 2013
Accepted 10 October 2013
Available online 19 October 2013

Keywords:
Lymph node metastasis
Photothermal therapy
Gold nanorods
Plasmon resonance

ABSTRACT

Lymph node dissection for regional nodal metastasis is a primary option, but is invasive and associated with adverse effects. The development of non-invasive therapeutic methods in preclinical experiments using mice has been restricted by the small lymph node size and the limited techniques available for non-invasive monitoring of lymph node metastasis. Here, we show that photothermal therapy (PTT) using gold nanorods (GNRs) and near-infrared (NIR) laser light shows potential as a non-invasive treatment for tumors in the proper axillary lymph nodes (proper-ALNs) of MXH10/Mo-*lpr/lpr* mice, which develop systemic swelling of lymph nodes (up to 13 mm in diameter, similar in size to human lymph nodes). Tumor cells were inoculated into the proper-ALNs to develop a model of metastatic lesions, and any anti-tumor effects of therapy were assessed. We found that GNRs accumulated in the tumor in the proper-ALNs 24 h after tail vein injection, and that irradiation with NIR laser light elevated tumor temperature. Furthermore, combining local or systemic delivery of GNRs with NIR irradiation suppressed tumor growth more than irradiation alone. We propose that PTT with GNRs and NIR laser light can serve as a new therapeutic method for lymph node metastasis, as an alternative to lymph node dissection.

1. Introduction

Regional lymph node dissection is considered a priority when tumor metastases are detected by imaging modalities (ultrasound, CT, MRI or PET) [1,2], provided that the lymph nodes are resectable and the patient fit for surgery [3]. However, this is a highly invasive procedure. Since the therapeutic efficacy of radiotherapy or chemotherapy is relatively low, novel, minimally-invasive treatments for lymph node metastasis are greatly needed.

Photothermal therapy (PTT) is less invasive than radiotherapy, chemotherapy and surgical management [4]. In PTT, optical energy is converted into heat by tissue absorption, causing irreversible tissue damage through thermal denaturing of proteins (and DNAs) and tissue coagulation [5]. Gold nanoparticles, which are non-toxic, non-immunogenic, stable and biocompatible [6], can facilitate PTT by absorbing light, and minimize collateral damage to normal tissue by accumulating near a tumor through bioconjugation [5]. Near-infrared (NIR) laser light has a 'therapeutic window' corresponding to a wavelength band that is minimally absorbed by the blood and soft tissues and does not excite autofluorescence [7]. Since NIR laser light can penetrate soft tissues to depths exceeding 5 cm [8], its combination with gold nanoparticles offers a novel treatment for cancer. Gold nanoparticles exist as varying structures, including nanocages [5], nanowires [9], silica-cored nanoshells and nanorods [10]. Gold nanorods (GNRs) have two surface plasmon absorption bands: a long-wavelength (800–900 nm) and weaker short-wavelength (~500 nm) band due to longitudinal and transverse oscillation of electrons, respectively [11]. The absorption maximum of the longitudinal band shifts to longer wavelengths with increasing aspect-ratio; by selecting GNRs with an aspect-ratio appropriate for the NIR wavelength, effective treatment of cancer may be possible. Several types of GNR have been developed to increase tumor selectivity and efficacy, including GNRs conjugated to the anti-epidermal growth factor receptor [11,12], polyacrylic acid-coated GNRs [13], doxorubicin-loaded GNRs [14] and GNRs conjugated

* Corresponding author at: Laboratory of Biomedical Engineering for Cancer, Graduate School of Biomedical Engineering, Tohoku University, 4-1 Seiryo, Aoba Ward, Sendai, Miyagi 980-8575, Japan. Tel./fax: +81 22 717 7583.
E-mail address: kodama@bme.tohoku.ac.jp (T. Kodama).

0168-3659/$ – see front matter © 2013 Elsevier B.V. All rights reserved.
http://dx.doi.org/10.1016/j.jconrel.2013.10.014

with arginine–glycine–aspartic acid peptides [15]. The selectivity of GNRs is improved further by the enhanced permeability and retention (ERP) effect [16].

In mice, PTT and GNRs have been assessed for the treatment of solid tumors [10,15,17–20], but not lymph node metastases, in part because the induction and detection of metastases in murine lymph nodes are challenging due to their small size (a few millimeters) [21]. Previously, we have used the MRL/MpJ-*lpr/lpr* (MRL/lpr) mouse as an animal model of lymph node metastasis, because its lymph nodes swell to a size similar to that in humans. However, the MRL/lpr strain is also utilized as a model of autoimmune diseases, and has the major disadvantage that lethal nephritis occurs at the same age (4–5 months) as lymph node swelling [22].

Recently, we developed a recombinant MXH10/Mo-*lpr/lpr* (MXH10/Mo/lpr) strain (by intercrossing MRL/lpr and C3H/HeJ-*lpr/lpr* mice) that shows widespread lymph node swelling at only 2.5–3 months of age, with lymph nodes as large as 10 mm; both the lymph node size and the onset of swelling are consistent and predictable. Moreover, these mice do not develop severe glomerulonephritis and vasculitis [23], and have a longer lifespan than MRL/lpr mice. Here, we have induced tumor development in the proper axillary lymph nodes (proper-ALNs) of MXH10/Mo/lpr mice, and evaluated the use of PTT in combination with GNRs for the treatment of these tumors.

2. Materials and methods

All *in vivo* studies were approved by the Institutional Animal Care and Use Committee of Tohoku University.

2.1. Gold nanorods

Bare gold nanorods (bareGNRs) (aspect ratio: 6.6; surface plasmon resonance (SPR) peak: 1050 nm; 30-HAR-1064) and neutravidin polymer-conjugated gold nanorods (GNRs) (aspect ratio: 6.7; SPR peak: 1065 nm; axial diameter: 10 nm; length: 67 nm; D12-1064-PN-50) were used (Nanopartz). Fluorescent GNRs (FluoGNRs) were prepared by conjugation (30 min, room temperature) of GNRs (12.4×10^{12} particles/mL in phosphate-buffered saline [PBS]) with Atto 590-biotin (excitation: 598 nm; emission: 624 nm; Sigma-Aldrich); excess dye was removed by three centrifugation (5000 ×*g*, 5 min) and washing steps. The zeta potentials of the GNRs (6.0×10^{10} particles/mL in distilled water) were measured (ELSZ-2 analyzer; Otsuka) as: bareGNRs, 46.54 ± 0.69 mV; GNRs, −13.79 ± 1.33 mV; and FluoGNRs, −16.65 ± 2.11 mV ($n = 3$ for each). GNR absorption spectra were measured using a UV-visible near-infrared spectrophotometer (V-7200; JASCO). FluoGNR configuration (6.0×10^{10} particles/mL in distilled water) was examined with a transmission electron microscope (HT7700; Hitachi) operated at 80 kV.

2.2. Cell culture

KM-Luc/GFP cells [1], which stably express a fusion of the luciferase (Luc) and enhanced-green fluorescent protein (EGFP) genes, were cultured in Complete Medium, consisting of Dulbecco's Modified Eagle Medium supplemented with 10% fetal bovine serum containing 1% L-glutamine–penicillin–streptomycin (Sigma-Aldrich) and 0.5% Geneticin G418 (Wako). The absence of *Mycoplasma* contamination was confirmed with a *Mycoplasma* detection kit (R&D Systems).

2.3. Mice

MXH10/Mo/lpr mice, established by intercrossing MRL/lpr and C3H/HeJ-*lpr/lpr* (C3H/lpr) strains [23], were bred and maintained at the Institute for Animal Experimentation, Graduate School of Medicine, Tohoku University. Seventy-six mice were used (weight, 25–35 g; age, 11–14 weeks). The longitudinal diameter of the proper-ALN, measured using a digital caliper, was 9.76 ± 0.35 mm ($n = 6$).

2.4. Induction of metastasis in the proper-ALN

Tumor development in mice ($n = 57$) was induced by injection into the proper-ALN of 3.3×10^5 KM-Luc/GFP cells/mL, suspended in a mixture of 10 μL PBS (Ca^{2+}- and Mg^{2+}-free) and 20 μL of 400 mg/mL Matrigel (Collaborative Biomedical Products), under the guidance of a high-frequency ultrasound imaging system (Vevo770; VisualSonics) with a 25 MHz transducer (RMV-710B). To measure the luciferase activities of tumors growing in the proper-ALNs, luciferin (150 mg/kg; Promega) was injected intraperitoneally under anesthesia (2% isoflurane in oxygen). 10 min after injection, luciferase bioluminescence was measured for 30 s using an *in vivo* luminescence imaging system (IVIS; Xenogen); this procedure was carried out on days 2, 3, 4, 5, 7 and 9 post-inoculation. The proper-ALN size was measured using an *in vivo* high-resolution three-dimensional microimaging system (VEVO770; VisualSonics) with a 25 MHz transducer (RMV-710B; axial resolution 70 μm, focal length 15 mm) set at 50% transmission power [24].

2.5. Blood biochemistry investigations

The toxicity of systemic GNR injection was evaluated using serum biochemistry tests. Four mice were injected intravenously with GNRs (12.4×10^{12} particles/mL, 100 μL), and four controls with PBS (100 μL). On day 17 after injection, blood samples from the caudal vena cava (taken under general anesthesia) were centrifuged (2000 ×*g*, 5 min) to obtain serum. Hepatic and renal injuries were evaluated from serum measurements of total bilirubin (T-BIL), alanine aminotransferase (ALT), aspartate aminotransferase (AST) and blood urea nitrogen (BUN) (Oriental Yeast).

2.6. GNR Biodistribution

Mice were injected intravenously with GNRs (12.4×10^{11} particles/mL) in PBS, and sacrificed after 12 h, 24 h or 17 days ($n = 3$ for each). Blood was drawn from the abdominal aorta, and the organs and tissues quickly removed and freeze-dried for 20 h. Samples in nitrohydrochloric acid were heated (160 °C for 5 min, 190 °C for 45 min), dispensed into 25 mL PBS, and analyzed for metal concentration by inductively-coupled plasma mass spectrometry (ICP-MS, HP4500, Hitachi). Values for each sample were divided by the quantity of GNRs injected to obtain a percentage (%).

2.7. NIR laser light irradiation

Laser light of 1.5 W/cm^2 from a continuous Nd: YVO4 air-cooled laser (1064 nm; beam diameter: TEM_{00}, 0.6 mm; CYD-010-TUBC; Neoarc) was delivered to the target site by an optical fiber (fiber diameter: 400 μm; collimator diameter: 20 mm). The collimator head was fixed to a three-dimensional stage control system (Mark-204-MS; Sigma Koki). The temperature at the irradiated site was measured by functional thermography (1.07 mrad spatial resolution, 0.05 °C minimum temperature resolution; TVS-500; Nippon Avionics).

2.8. Treatment of tumors in the proper-ALNs with PTT

To evaluate the anti-tumor effects of laser irradiation (1.5 W/cm^2, 180 s) and local/systemic GNR delivery, luciferase activities of tumors in the proper-ALNs were measured on days 2, 3, 4, 5, 7 and 9 after tumor inoculation. The proper-ALN volume was measured on days 0, 6 and 9 (Vevo770 high-frequency ultrasound system). Based on studies of human skin burns, the possible occurrence of skin burning was evaluated through macroscopic observations of redness, blistering, ulceration, and full-thickness necrosis of the skin.

2.8.1. Local delivery of GNRs

In the control group ($n = 6$), 30 μL saline was injected intranodally on days 3 and 4 after tumor inoculation. In the GNRs group ($n = 6$), 30 μL GNRs (3.6×10^{12} GNRs/mL) was injected into the proper-ALN on day 3. In the laser group ($n = 6$), the proper-ALN was injected with 30 μL PBS on day 3, and irradiated with NIR light on days 3 and 4. In the laser + GNRs group ($n = 6$), the proper-ALN was injected with 30 μL GNRs (3.6×10^{12} GNRs/mL) on day 3, and irradiated with NIR light on days 3 and 4.

2.8.2. Systemic delivery of GNRs

In the control group ($n = 6$), 100 μL saline was injected intravenously on day 2. In the GNRs group ($n = 6$), 100 μL GNRs in saline (14.4×10^{12} GNRs/mL) was injected intravenously. In the laser group ($n = 6$), 100 μL saline was injected intravenously, and the proper-ALNs irradiated with NIR light on days 3 and 4. In the laser + GNRs group ($n = 6$), 100 μL GNRs in saline (14.4×10^{12} GNRs/mL) was injected intravenously, and the proper-ALNs irradiated with NIR light on days 3 and 4.

2.9. Histological analysis

Frozen sections of lymph nodes were fixed (4% paraformaldehyde, 15 min, room temperature) and washed (PBS). The cytotoxic area was analyzed following hematoxylin and eosin (HE), 4′,6-diamidino-2-phenylindole (DAPI) and CD31 staining. For CD31 staining, purified rat anti-mouse CD31 primary antibody (MED13.3; BD Pharmingen) was diluted (1:100) in PBS with 3% bovine serum albumin and 0.1% Triton-X, and applied overnight at 4 °C. After washing (PBS), the slides were incubated (40 min, 4 °C) with Alexa 488-conjugated goat anti-rat secondary antibody (1:500; Life Technologies) and DAPI (100 ng/mL). After washing (PBS), sections were mounted with Vectorshield (Vector). Histological images were captured using a fluorescence microscope (BX51; Olympus), digital camera (DP72; Olympus) and Photoshop CS3 (Adobe). For paraffin-embedded samples, harvested lymph nodes were fixed overnight (10% formaldehyde, 4 °C; Rapid Fixative; Kojima Chemical Industry), dehydrated, embedded in paraffin, sectioned (2–4 μm serial sections), stained with HE, and analyzed using a microscope (BX51; Olympus) and digital camera (DP72; Olympus).

2.10. Statistical analysis

Data are presented as the mean ± SD or SEM. Statistical differences were analyzed using the Kruskal–Wallis and Steel tests. $P < 0.05$ was considered indicative of statistical significance.

3. Results

First, we investigated GNR biodistribution 12 h, 24 h and 17 days after intravenous injection ($n = 3$) (Fig. 1A). The GNR level (% initial dose) in the liver was 30–40% at each time point, with much lower accumulation in the spleen and kidney. Accumulation in the proper-ALN was approximately 0.01% at 24 h with tumor present, but negligible in the absence of tumor. Accumulation of FluoGNRs in the tumor was confirmed by fluorescence microscopy: Fig. 1Ba shows representative HE staining, and Fig. 1Bb presents a corresponding image with nuclei stained by DAPI, CD31-positive cells stained green, and FluoGNRs detected as red. Table 1 shows the evaluation of GNR toxicity (17 days after injection) from changes in body weight and serum biochemistry investigations. There were no significant differences in body weight and serum T-BIL, ALT, AST and BUN between control mice and those administered GNRs.

Next, we investigated the effect of laser light irradiation on tumors in lymph nodes, compared with local and systemic delivery of GNRs. Fig. 2A shows representative thermographic images of proper-ALNs containing tumors: the local rise in temperature induced by laser irradiation was further increased by GNR administration, with local

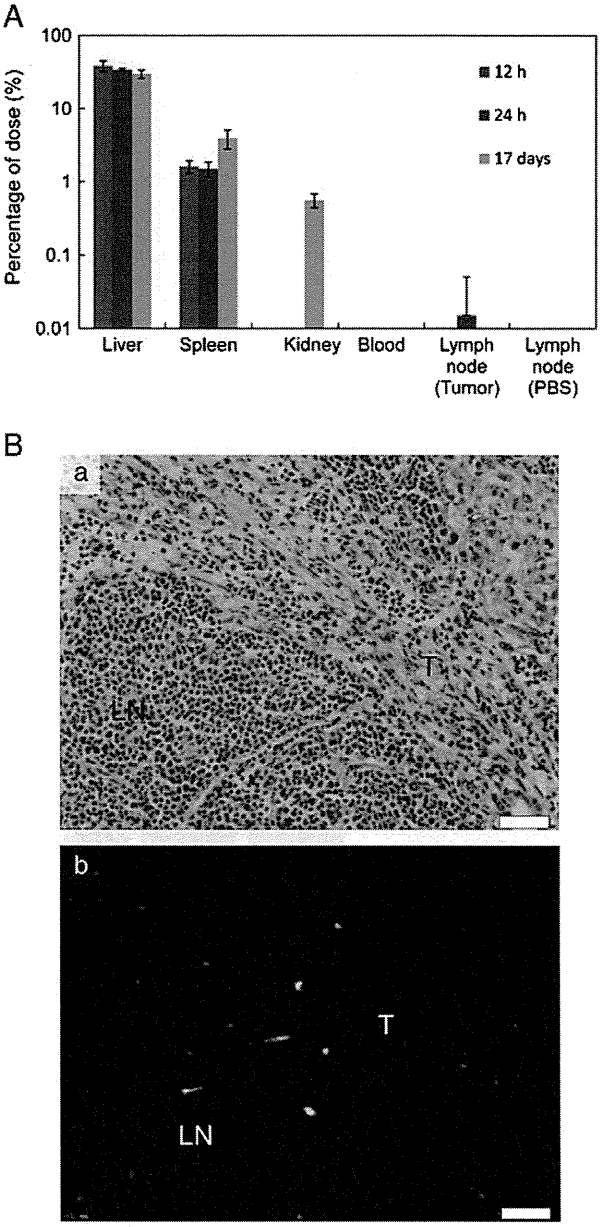

Fig. 1. Uptake of GNRs into organs. A. Biodistribution of the GNRs, injected intravenously 2 days after tumor inoculation into the proper-ALNs. GNR uptake into organs was measured 12 h, 24 h and 17 days after injection. Hepatic uptake was significantly higher than that of other organs. GNR uptake into the tumor in the proper-ALNs was detected 24 h after injection. Mean ± SD values are shown ($n = 3$). B. Histological analysis of the proper-ALNs containing tumor. (a) HE staining, (b) overlay image. GNRs are evident in the tumor mass, independent of CD31-positive blood vessels. Blue: nuclei stained with DAPI; green: CD31-positive cells (Ex: 495 nm, Em: 520 nm); red: FluoGNRs (Ex: nm, Em: nm). Scale bar = 40 μm. T: spindle-shaped tumor cells growing invasively into lymph node tissue; LN: intact lymph node tissue.

delivery of GNRs slightly superior to systemic delivery. Fig. 2B illustrates the increment in the maximum temperature from $\Delta T = 0$ (36 °C): the temperature at 3 min reached 46 °C for laser irradiation alone, 51 °C for laser irradiation + GNRs (local delivery), and 50 °C for laser irradiation + GNRs (systemic delivery).

The cytoreductive effects of PTT were assessed using bioluminescence imaging and high-frequency ultrasound systems. Fig. 3A presents the changes in luciferase activities over time. Compared with the control group, the luciferase activities of the laser + GNRs groups (both local and systemic) were significantly lower on day 4, and that of the laser + GNRs (local) group was significantly lower on day 5 ($P < 0.05$,

Table 1
Evaluation of GNR toxicity.

	Control	GNRs	Statistical significance
T-BIL (mg/dL)	0.05 ± 0.01	0.03 ± 0.01	NS
ALT (IU/L)	69.75 ± 8.06	58.75 ± 8.61	NS
AST (IU/L)	172.67 ± 16.94	155.25 ± 19.93	NS
BUN (mg/dL)	32.00 ± 3.02	49.98 ± 13.32	NS
Body weight change (g)	2.80 ± 0.43	1.75 ± 1.38	NS

Blood samples were obtained on day 17. Values represent the mean ± SEM ($n = 4$). NS, not significant; T-BIL, total bilirubin; ALT, alanine aminotransferase; AST, aspartate aminotransferase; BUN; blood urea nitrogen.

Steel test). Although irradiation with laser light was carried out on days 3 and 4 for both local and systemic GNR delivery, tumor growth was inhibited up to day 9 (Fig. 3A and B). As shown in Fig. 3C and D, the proper-ALN size increased approximately 2-fold over the 9-day study period in the control group; this is consistent with the normal lymph node tissue of the proper-ALN being partially replaced by infiltrating tumor cells, resulting in a noticeable, but not substantial, increase in the proper-ALN size. However, the proper-ALN size did not change significantly in the laser + GNRs (systemic) group (Steel test) (Fig. 3C and D), despite the fact that the luciferase activity was increased (Fig. 3A). This suggests that tumor necrosis following the administration of laser light and GNRs limited the volume growth of the lymph node.

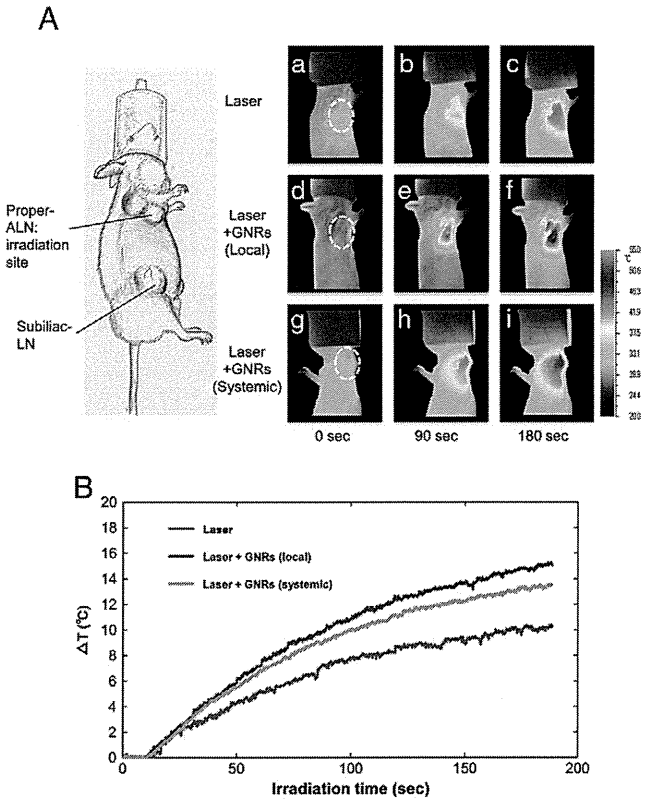

Fig. 2. Laser irradiation of tumors in the proper-ALNs. A. Anatomical and thermographic images of tumors in the proper-ALNs, irradiated on day 3. (a, b, c): laser light alone; (d, e, f): laser light with local GNR delivery; (g, h, i): laser light with systemic GNR delivery. (a, d, g): irradiation time 0 s; (b, e, h): irradiation time 90 s; (c, f, i): irradiation time 180 s. The dashed regions in (a), (d) and (g) indicate proper-ALN regions. The longitudinal diameter of the proper-ALN, measured using a digital caliper, was 9.76 ± 0.35 mm ($n = 6$). B. Increment in the maximum temperature, from $\Delta T = 0$ (36 °C), against time, measured by thermography. At 3 min, the temperature reached 46 °C for laser irradiation alone, and approximately 51 °C for laser irradiation with GNRs (either local or systemic).

The assessment of skin burning revealed that there were no obvious skin lesions in the laser alone group, full-thickness necrosis of the skin in 33.3% of the laser + GNRs (systemic) group, and full-thickness necrosis of the skin in all animals of the laser + GNRs (local) group. The extent of the tissue damage induced by each treatment method was assessed using histological techniques. NIR laser light was irradiated in the direction of the arrows shown in Fig. 4. Lymph nodes of the control group, which had been inoculated with tumor cells, demonstrated progressive proliferation and invasion of spindle-shaped tumor cells (Fig. 4A,B,C). In lymph nodes treated with laser irradiation alone, both lymphatic tissue and tumor in the irradiated area showed evidence of coagulative necrosis, characterized by nuclear debris and pyknotic cells surrounded by an eosinophilic necrotic mass at the periphery (Fig. 4D,E,F). However, proliferation of tumor cells was still discernible outside the area of irradiation (Fig. 4F). Lymph nodes treated locally with GNRs plus laser irradiation also showed a localized region of necrosis (Fig. 4G,H,I), although this seemed more extensive than that with laser irradiation alone (Fig. 4G). In lymph nodes treated with systemic administration of GNRs plus laser irradiation, the findings were similar to those observed with local GNR delivery (Fig. 4J,K,L).

4. Discussion

The present study is the first to show, in MXH10/Mo/lpr mice that develop systemic swelling of lymph nodes to sizes similar to those in humans, that lymph node metastasis may be treated with PTT consisting of NIR laser light and GNRs. The anti-tumor effects of PTT with systemic delivery of GNRs (injection into the tail vein), as indicated by changes in the luciferase activity, were smaller than those achieved using local delivery (injection into the proper-ALN), but larger than those of NIR laser irradiation alone. A significant anti-tumor effect was observed on day 3, followed by an inhibition of tumor growth (Fig. 3A and B). This inhibition of tumor growth was achieved with accumulation in the proper-ALN of only 0.01% of the total GNR dose administered, with most of the GNRs accumulating into non-target sites such as the liver, spleen and reticuloendothelial system for 17 days without severe side effect (Fig. 1, Table 1) [25]. It is notable that the change in lymph node volume, as shown in Fig. 3C and D, does not serve as a sensitive parameter of the anti-tumor effect, as compared with luciferase activity. This is partly because the normal lymph node tissue is partially replaced by infiltrating tumor cells, causing only a slight increase in nodal size [1], and partly because necrosis of tumor cells by laser irradiation does not contribute substantially to a decrease in lymph node volume over a short period of time.

In the present study, tumor cells were injected into the proper-ALNs so that they subsequently developed in the lymph node as a solid tumor. However, in the establishment of metastasis in a patient with a malignant tumor, the tumor cells metastasize into the marginal sinus *via* the afferent lymphatic vessel, and invade into the cortex and paracortex, and then into the medulla [1]. Furthermore, blood vessels in non-metastatic lymph nodes may increase in size and number, while lymph vessels in the region of non-metastatic lymph nodes decrease their total size and may collapse due to the expanding primary tumor [1]. Therefore, the accumulation of GNRs and the subsequent anti-tumor effect observed in the present study may differ from that which would occur in lymph nodes with a true metastatic tumor. Thus, the anti-tumor actions of PTT with GNRs on lymph nodes with true metastases require further investigation.

The tumor in the lymph node was irradiated with NIR laser light at 1.5 W/cm^2 for 3 min. Laser irradiation alone increased the temperature in the proper-ALN to more than 46 °C, while the addition of local and systemic delivery of GNRs resulted in temperature rises to over 50 °C (Fig. 2B). Thermal damage occurs up to a depth of 10 mm (Fig. 4) [26]. It was notable that the temperature increment was similar for local and systemic injection of GNRs (Fig. 2), despite the fact that local injection would be expected to result in a higher concentration of

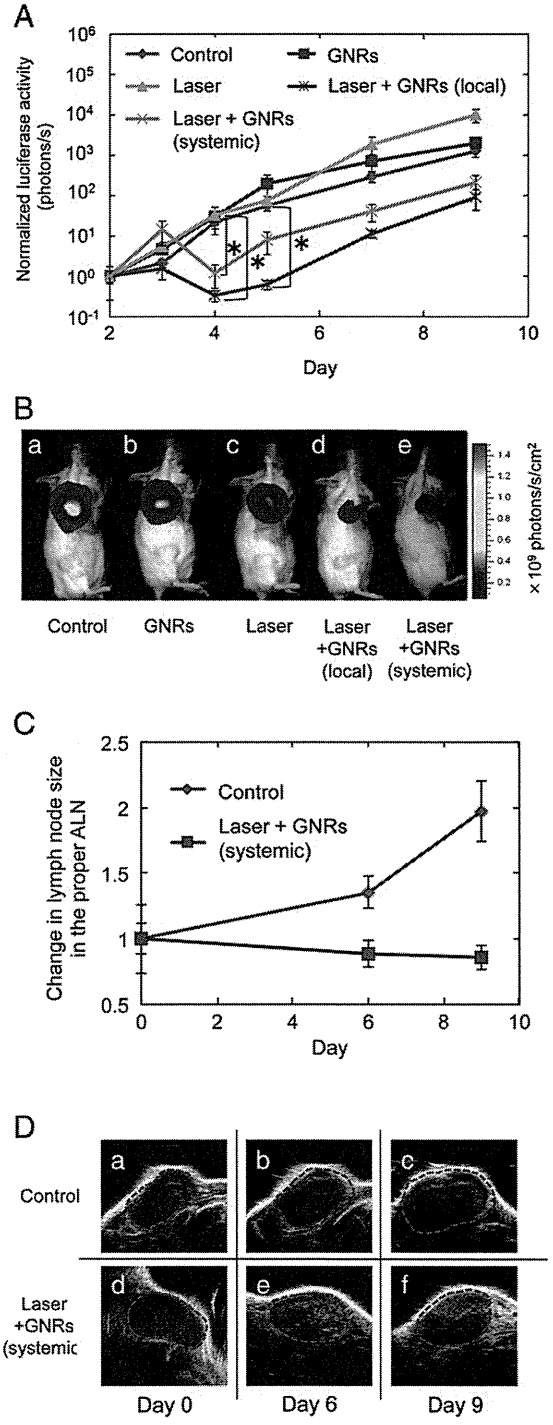

Fig. 3. *In vivo* anti-tumor effects of NIR laser light and GNRs. A. Luciferase activities (bioluminescence imaging) in the proper-ALNs, normalized to that on day 2. Significant differences between groups (* $P < 0.05$, Steel test) were detected on day 4 (control *vs.* laser + GNRs [local]; control *vs.* laser + GNRs [systemic]) and day 5 (control *vs.* laser + GNRs [local]). Mean ± SD values are shown ($n = 6$). B. Representative images of the tumor in the proper-ALN observed using an *in vivo* bioluminescence imaging system on day 9. C. Changes in the proper-ALN size over time in the control and laser + GNRs (systemic) groups, assessed using three-dimensional high-frequency ultrasound. The values were normalized to those on day 0. On days 6 and 9, lymph node size had increased in the control group, but not in the laser + GNRs (systemic) group. Mean ± SD values are shown ($n = 6$). D. Two-dimensional high-frequency ultrasound images, showing temporal changes in the lymph node size in the control and laser + GNRs (systemic) groups. The dashed regions indicate proper-ALN regions.

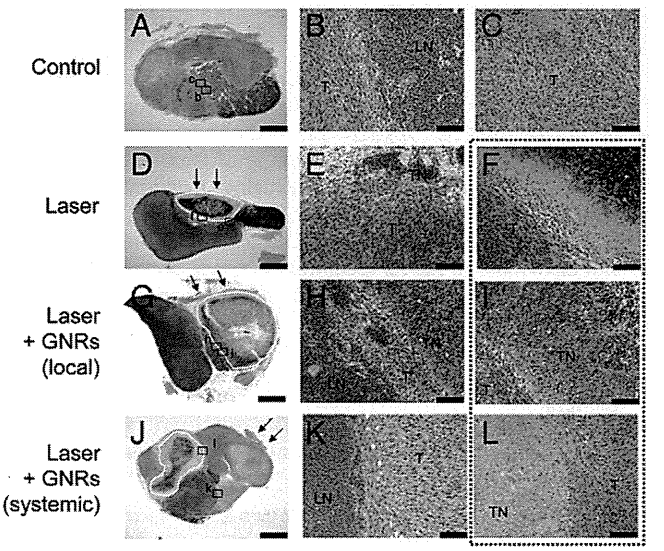

Fig. 4. Histochemical features. The lymph node inoculated with tumor cells and not treated with PTT (control) showed progressive proliferation and invasion of spindle-shaped tumor cells (A, B, C). The node treated by laser irradiation alone (laser) showed coagulative necrosis in the irradiated area, with nuclear debris and pyknotic cells surrounded by an eosinophilic necrotic mass (D, E, F). Outside the area of laser irradiation, tumor cell proliferation was discernible (F). The node treated by local GNR injection plus laser irradiation (laser + GNRs [local]) showed similar necrosis (G, H, I), although the necrotic area was more extensive than that of the lymph node treated with laser irradiation alone (G). In the lymph node treated by systemic GNR administration plus laser irradiation (laser + GNRs [systemic]), the histopathological findings were similar to those for local GNR injection (J, K, L), although the entire irradiated area showed extensive necrosis of lymphatic tissue and tumor; nonetheless, residual viable tumor cells remained. Sections were stained with HE on day 9 after tumor inoculation into the proper-ALNs. The boxed areas in (A), (D), (G), (J) are presented at higher magnification in the middle and right panels. Arrows: direction of the NIR laser light. Bar (left to right): 2 mm, 100 μm, 100 μm. T: tumor; TN: tumor necrosis; LN: lymph node tissue. The solid regions in (D), (G) and (J) indicate TN regions. The dashed line circumscribing (F), (I) and (L) highlights images containing T and TN regions.

GNRs. This is likely due to the characteristics of thermography, which is limited to measuring the surface temperature of the material. Thus, even if the amount of heat generated deeper in the structure was different between systemic and local injection of GNRs, this difference could not be measured with thermography. In addition, heat flow from inside the lymph node to the surface is inhibited by the blood flow in the skin, limiting the increase in the surface temperature.

The assessment of skin burning showed no obvious skin lesions for laser alone, full-thickness necrosis of the skin in 33.3% of the laser + GNRs (systemic) group, and full-thickness necrosis of the skin in all animals of the laser + GNRs (local) group, indicating that GNRs may have leaked into the tissue close to the skin. Alternatively, the dose of GNRs administered may influence the occurrence of burns. However, despite the increased temperature and resulting irreversible tissue damage, the tumor was not completely destroyed as viable tumor cells were found to regrow. In order to develop a more effective therapy, a novel irradiation method should be developed that is able to treat deep tumors without skin damage, possibly by employing active cooling of the skin surface.

5. Conclusion

We have demonstrated the potential of PTT, using systemic or local delivery of GNRs together with only two applications of NIR laser light, to treat tumors in the proper-ALN. Future studies optimizing the characteristics of the GNRs, and the methods used for the delivery of GNRs and laser irradiation, may allow for the development of an effective and minimally invasive treatment for metastatic lesions.

Acknowledgments

This study was supported by a Grant for the World Center of Education and Research for Trans-disciplinary Flow Dynamics, Tohoku University Global COE Program, and a Grant for the Collaborative Research Project (J13094) of the Institute of Fluid Science, Tohoku University, a Grant-in-Aid for Challenging Exploratory Research (24659884, 24650286), and a Grant-in-Aid for Scientific Research (B) (23300183, 25293382). The authors thank M. Ono and M. Nose for helpful discussion, N. Sax for technical assistance, and the Biomedical Research Core of Tohoku University Graduate School of Medicine for technical support.

References

[1] L. Li, S. Mori, M. Kodama, M. Sakamoto, S. Takahashi, T. Kodama, Enhanced sonographic imaging to diagnose lymph node metastasis: importance of blood vessel volume and density, Cancer Res. 73 (2013) 2082–2092.
[2] I.J. Robertson, F. Hand, M.R. Kell, FDG-PET/CT in the staging of local/regional metastases in breast cancer, Breast 20 (2011) 491–494.
[3] J.E. Gershenwald, M.I. Ross, Sentinel-lymph-node biopsy for cutaneous melanoma, N. Engl. J. Med. 364 (2011) 1738–1745.
[4] A.M. Alkilany, L.B. Thompson, S.P. Boulos, P.N. Sisco, C.J. Murphy, Gold nanorods: their potential for photothermal therapeutics and drug delivery, tempered by the complexity of their biological interactions, Adv. Drug Deliv. Rev. 64 (2012) 190–199.
[5] J. Chen, D. Wang, J. Xi, L. Au, A. Siekkinen, A. Warsen, Z.Y. Li, H. Zhang, Y. Xia, X. Li, Immuno gold nanocages with tailored optical properties for targeted photothermal destruction of cancer cells, Nano Lett. 7 (2007) 1318–1322.
[6] J. You, R. Zhang, G. Zhang, M. Zhong, Y. Liu, C.S. Van Pelt, D. Liang, W. Wei, A.K. Sood, C. Li, Photothermal-chemotherapy with doxorubicin-loaded hollow gold nanospheres: a platform for near-infrared light-trigged drug release, J. Control. Release 158 (2012) 319–328.
[7] W.S. Kuo, Y.T. Chang, K.C. Cho, K.C. Chiu, C.H. Lien, C.S. Yeh, S.J. Chen, Gold nanomaterials conjugated with indocyanine green for dual-modality photodynamic and photothermal therapy, Biomaterials 33 (2012) 3270–3278.
[8] G. Ku, L.V. Wang, Deeply penetrating photoacoustic tomography in biological tissues enhanced with an optical contrast agent, Opt. Lett. 30 (2005) 507–509.
[9] H.K. Moon, M. Son, J.E. Park, S.M. Yoon, S.H. Lee, H.C. Choi, Significant increase in the water dispersibility of zinc phthalocyanine nanowires and applications in cancer phototherapy, NPG Asia Mater. 4 (2012) e12.
[10] G. von Maltzahn, J.H. Park, A. Agrawal, N.K. Bandaru, S.K. Das, M.J. Sailor, S.N. Bhatia, Computationally guided photothermal tumor therapy using long-circulating gold nanorod antennas, Cancer Res. 69 (2009) 3892–3900.
[11] X. Huang, I.H. El-Sayed, W. Qian, M.A. El-Sayed, Cancer cell imaging and photothermal therapy in the near-infrared region by using gold nanorods, J. Am. Chem. Soc. 128 (2006) 2115–2120.
[12] X. Huang, I.H. El-Sayed, W. Qian, M.A. El-Sayed, Cancer cells assemble and align gold nanorods conjugated to antibodies to produce highly enhanced, sharp, and polarized surface Raman spectra: a potential cancer diagnostic marker, Nano Lett. 7 (2007) 1591–1597.
[13] J. Wang, B. Dong, B. Chen, Z. Jiang, H. Song, Selective photothermal therapy for breast cancer with targeting peptide modified gold nanorods, Dalton Trans. 41 (2012) 11134–11144.
[14] S. Shen, H. Tang, X. Zhang, J. Ren, Z. Pang, D. Wang, H. Gao, Y. Qian, X. Jiang, W. Yang, Targeting mesoporous silica-encapsulated gold nanorods for chemo-photothermal therapy with near-infrared radiation, Biomaterials 34 (2013) 3150–3158.
[15] G.P. Goodrich, L. Bao, K. Gill-Sharp, K.L. Sang, J. Wang, J.D. Payne, Photothermal therapy in a murine colon cancer model using near-infrared absorbing gold nanorods, J. Biomed. Opt. 15 (2010) 018001.
[16] Y. Matsumura, H. Maeda, A new concept for macromolecular therapeutics in cancer chemotherapy: mechanism of tumoritropic accumulation of proteins and the anti-tumor agent smancs, Cancer Res. 46 (1986) 6387–6392.
[17] J.T. Robinson, K. Welsher, S.M. Tabakman, S.P. Sherlock, H. Wang, R. Luong, H. Dai, High performance *in vivo* near-IR (>1 mum) imaging and photothermal cancer therapy with carbon nanotubes, Nano Res. 3 (2010) 779–793.
[18] A.J. Gormley, K. Greish, A. Ray, R. Robinson, J.A. Gustafson, H. Ghandehari, Gold nanorod mediated plasmonic photothermal therapy: a tool to enhance macromolecular delivery, Int. J. Pharm. 415 (2011) 315–318.
[19] X.F. Yu, Z. Sun, M. Li, Y. Xiang, Q.Q. Wang, F. Tang, Y. Wu, Z. Cao, W. Li, Neurotoxin-conjugated upconversion nanoprobes for direct visualization of tumors under near-infrared irradiation, Biomaterials 31 (2010) 8724–8731.
[20] M. Jaunich, S. Raje, K. Kim, K. Mitra, Z.X. Guo, Bio-heat transfer analysis during short pulse laser irradiation of tissues, Int. J. Heat Mass Transfer 51 (2008) 5511–5521.
[21] L. Li, S. Mori, M. Sakamoto, S. Takahashi, T. Kodama, Mouse model of lymph node metastasis via afferent lymphatic vessels for development of imaging modalities, PLoS ONE 8 (2013) e55797.
[22] E.D. Murphy, J.B. Roths, Autoimmunity and lymphoproliferation: induction by mutant gene lpr, and acceleration by a male-associated factor in strain BXSB mice, Elsevier/North-Holland, New York, 1978.
[23] L. Shao, S. Mori, Y. Yagishita, T. Okuno, Y. Hatakeyama, T. Sato, T. Kodama, Lymphatic mapping of mice with systemic lymphoproliferative disorder: usefulness as an inter-lymph node metastasis model of cancer, J. Immunol. Methods 389 (2013) 69–78.
[24] T. Kodama, N. Tomita, Y. Yagishita, S. Horie, K. Funamoto, T. Hayase, M. Sakamoto, S. Mori, Volumetric and angiogenic evaluation of antitumor effects with acoustic liposome and high-frequency ultrasound, Cancer Res. 71 (2011) 6957–6964.
[25] N. Khlebtsov, L. Dykman, Biodistribution and toxicity of engineered gold nanoparticles: a review of *in vitro* and *in vivo* studies, Chem. Soc. Rev. 40 (2011) 1647–1671.
[26] L.R. Hirsch, R.J. Stafford, J.A. Bankson, S.R. Sershen, B. Rivera, R.E. Price, J.D. Hazle, N.J. Halas, J.L. West, Nanoshell-mediated near-infrared thermal therapy of tumors under magnetic resonance guidance, Proc. Natl. Acad. Sci. U. S. A. 100 (2003) 13549–13554.

Cell PRESS

Immunity
Article

Enhanced Apoptosis by Disruption of the STAT3-IκB-ζ Signaling Pathway in Epithelial Cells Induces Sjögren's Syndrome-like Autoimmune Disease

Atsushi Okuma,[1] Katsuaki Hoshino,[2,3,9] Tomoyuki Ohba,[1] Sawako Fukushi,[5] Setsuya Aiba,[5] Shizuo Akira,[4,7] Masao Ono,[6] Tsuneyasu Kaisho,[2,3] and Tatsushi Muta[1,8,*]

[1]Laboratory of Cell Recognition and Response, Graduate School of Life Sciences, Tohoku University, Sendai, Miyagi 980-8578, Japan
[2]Laboratory for Host Defense, RIKEN Research Center for Allergy and Immunology, Yokohama, Kanagawa 230-0045, Japan
[3]Laboratory for Immune Regulation
[4]Laboratory of Host Defense
World Premier International Immunology Frontier Research Center, Osaka University, Suita, Osaka 565-0871, Japan
[5]Department of Dermatology
[6]Department of Pathology
Tohoku University Graduate School of Medicine, Sendai, Miyagi 980-8575, Japan
[7]Research Institute for Microbial Diseases, Osaka University, Suita, Osaka 565-0871, Japan
[8]Global Center of Excellence Program, Center for Ecosystem Management Adapting to Global Change, Sendai, Miyagi 980-8578, Japan
[9]Present address: Department of Immunology, Faculty of Medicine, Kagawa University, Miki, Kagawa 761-0793, Japan
*Correspondence: tmuta@biology.tohoku.ac.jp
http://dx.doi.org/10.1016/j.immuni.2012.11.016

SUMMARY

Sjögren's syndrome (SS) is an autoimmune disease characterized by exocrinopathy that leads to dry eye and mouth. Although lymphocyte infiltration into exocrine glands and the generation of autoantibodies have been reported in SS, its pathogenic mechanism remains elusive. Here, we show that mice lacking the transcriptional regulator IκB-ζ developed SS-like inflammation characterized by lymphocyte-infiltrated dacryoadenitis and SS-associated autoantibodies. In particular, epithelial cells, but not hematopoietic cells, lacking IκB-ζ were essential for the development of inflammation. IκB-ζ-deficient epithelial cells in the lacrimal glands exhibited enhanced apoptosis even in the absence of lymphocytes. Administration of caspase inhibitors ameliorated the inflammation, indicating the critical role of caspase-mediated apoptosis. Furthermore, epithelial cell-specific STAT3-deficient mice developed SS-like inflammation with impaired IκB-ζ expression in the lacrimal glands. Thus, this study reveals a pathogenic mechanism of SS in which dysfunction of epithelial cells caused by disruption of STAT3-mediated IκB-ζ induction elicits the activation of self-reactive lymphocytes.

INTRODUCTION

A diverse array of genetic and environmental factors is involved in the pathogenesis of autoimmune diseases, which are the subject of intense investigation. Sjögren's syndrome (SS) is a major autoimmune disease that is characterized by ocular and oral dryness and affects 0.5% of the population (Fox, 2005). Functional impairment of exocrine glands such as the salivary and lacrimal glands is caused by autoimmune attack of epithelial tissues by infiltrating lymphocytes; thus, SS is occasionally referred to as autoimmune epithelitis (Mitsias et al., 2006). Patients with SS frequently generate autoantibodies against SS antigen A (SSA)/Ro and SS antigen B (SSB)/La, and therefore the presence of these autoantibodies is widely used for the clinical diagnosis of SS (Mavragani et al., 2000; Vitali et al., 2002). These autoantigens are ubiquitously expressed ribonucleoproteins (Mavragani et al., 2000), so the localization of the antigens does not account for the tissue-specific lesions. Additionally, accelerated apoptosis (Manganelli and Fietta, 2003; Matsumura et al., 1998; Nakamura et al., 1998; Polihronis et al., 1998) or enhanced expression of MHC class II (Moutsopoulos et al., 1986) or costimulatory (Manoussakis et al., 1999) molecules in the salivary or lacrimal glands has been reported in SS patients. Furthermore, several mouse models of SS indicate that the aberrant activation of lymphocytes may elicit SS (Groom et al., 2002; Li et al., 2004; Peng et al., 2010). However, the pathogenic mechanisms of primary SS remain elusive because lymphocyte activation possibly leads to apoptosis of epithelial cells and vice versa. Therefore, the relationship between the cause and the consequence needs to be clarified.

IκB-ζ, encoded by the *Nfkbiz* gene, is a member of the nuclear IκB family of proteins that acts as a transcriptional regulator via association with NF-κB (Yamazaki et al., 2001). Little IκB-ζ is detectable in unstimulated cells but IκB-ζ is robustly induced upon stimulation of Toll-like receptors (TLRs) or interleukin-1 (IL-1) receptor via transcriptional and posttranscriptional activation (Eto et al., 2003; Watanabe et al., 2007; Yamamoto et al., 2004; Yamazaki et al., 2001, 2005). IκB-ζ is essential for the induction of a subset of secondary response genes represented by the proinflammatory cytokine IL-6 in response to various TLR ligands in macrophages or fibroblasts (Motoyama et al., 2005; Yamamoto et al., 2004). IκB-ζ is also induced in lymphocytes

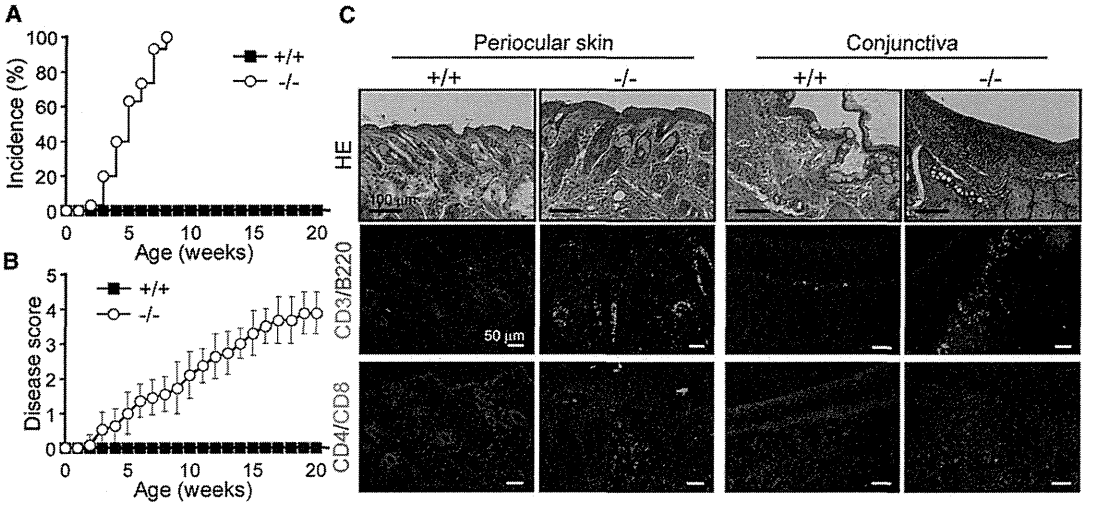

Figure 1. *Nfkbiz*$^{-/-}$ Mice Develop Lymphocyte-Dependent Chronic Inflammation

(A and B) Incidence and progression of the inflammation in *Nfkbiz*$^{-/-}$ (−/−) and *Nfkbiz*$^{+/+}$ (+/+) littermate control mice. Pathological phenotypes were scored as in Figure S1A after birth (n = 30). Incidence of the disease (score ≥ 1) is expressed as a percentage. The disease scores are shown as mean ± SD.

(C) Histology of the periocular skin and conjunctiva of 5-month-old *Nfkbiz*$^{-/-}$ and *Nfkbiz*$^{+/+}$ littermate mice. Sections of periocular skin and conjunctiva were stained with hematoxylin and eosin (HE) or immunostained with either CD3 (green) and B220 (red) antibodies or CD8 (green) and CD4 (red) antibodies. The nuclei were stained with DAPI (blue).

See also Figure S1.

upon antigen receptor stimulation (Hijioka et al., 2007; Okamoto et al., 2010). IκB-ζ induction in CD4$^+$ T cells is required for efficient T helper 17 (Th17) cell differentiation and therefore IκB-ζ-deficient mice are resistant to experimental autoimmune encephalomyelitis (Okamoto et al., 2010).

Despite impaired Th17 cell generation, IκB-ζ-deficient mice spontaneously develop severe inflammation in the conjunctiva and periocular skin (Ueta et al., 2005; Yamamoto et al., 2004). Although Th2 cell-polarized IL-4-mediated allergy was suspected in the mice (Shiina et al., 2004), it is unlikely because mutant mice lacking both IκB-ζ and STAT6, in which IL-4 signaling is abrogated, similarly developed inflammation (Ueta et al., 2008). In this study, we showed that IκB-ζ-deficient mice developed an SS-like autoimmune disease. IκB-ζ deficiency in hematopoietic cells was not essential for disease development. Instead, enhanced apoptosis in IκB-ζ-deficient epithelial tissue preceded lymphocyte infiltration, which culminated in inflammation. These results reveal a previously unknown role for IκB-ζ in the homeostasis of epithelial tissues and a possible molecular mechanism for the pathogenesis of SS.

RESULTS

Development of Inflammation in IκB-ζ-Deficient Mice Requires Lymphocytes

IκB-ζ-deficient (*Nfkbiz*$^{-/-}$) mice spontaneously develop conjunctivitis and periocular dermatitis under specific-pathogen-free conditions (Yamamoto et al., 2004). Eyelid swelling was detected in some *Nfkbiz*$^{-/-}$ mice as early as 2 weeks after birth, and the inflammatory changes became evident in all mutant mice by 8 weeks regardless of sex (Figures 1A and 1B; Figure S1A available online). Dermatitis in *Nfkbiz*$^{-/-}$ mice was localized primarily at the periocular region and progressively extended to the whole face, presenting as erosion and loss of hair. Disease scoring based on the inflamed area and the severity of inflammation indicated that the clinical manifestation was gradually exacerbated until around 20 weeks.

It has been reported that several mutant mice in which NF-κB function in the epidermis is dysregulated develop inflammation of the skin (Nenci et al., 2006; Omori et al., 2006; Pasparakis et al., 2002; Rebholz et al., 2007). Because the inflammation in those mutant mice was dependent on tumor necrosis factor (TNF), we crossed *Nfkbiz*$^{-/-}$ mice with *Tnf*$^{-/-}$ mice (Taniguchi et al., 1997) to generate *Nfkbiz*$^{-/-}$*Tnf*$^{-/-}$ mice. Interestingly, *Nfkbiz*$^{-/-}$*Tnf*$^{-/-}$ mice developed inflammation similar to that seen in *Nfkbiz*$^{-/-}$ mice (Figures S1B–S1E), indicating that TNF-α is dispensable for the inflammation, and hence the pathology of the inflammation in *Nfkbiz*$^{-/-}$ mice is distinct from inflammation observed in the previously described mutant mice.

Immunohistochemical analysis revealed heavy infiltration of lymphocytes in the dermis of the inflamed skin in *Nfkbiz*$^{-/-}$ mice (Figure 1C). In addition to T cells, infiltration of B cells was observed in the conjunctiva in mutant mice. The majority of the infiltrating T cells were of the CD4$^+$ T cell subset. In contrast to infectious or hypersensitive lesions, infiltration of myeloid cells, such as neutrophils and eosinophils, was scarcely observed in this lesion (Figure S1F).

As the inflammation progressed, *Nfkbiz*$^{-/-}$ mice exhibited splenomegaly and lymphadenopathy with greatly increased numbers of T and B cells (Figures S1G–S1I). CD44^{hi} memory or activated T cells were increased in the cervical lymph nodes of the *Nfkbiz*$^{-/-}$ mice compared to wild-type littermates (Figures S1J and S1K). Intracellular cytokine staining for interferon-γ and IL-17 revealed that Th1 cell-type response, rather than

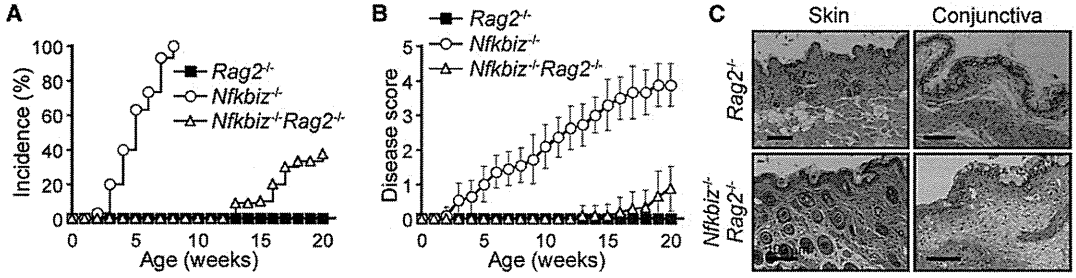

Figure 2. Lymphocytes Are Critical for the Development of Inflammation

(A and B) Incidence and progression of inflammation in *Nfkbiz*$^{-/-}$, *Rag2*$^{-/-}$, and *Nfkbiz*$^{-/-}$*Rag2*$^{-/-}$ mice. Incidence and disease score of littermate *Rag2*$^{-/-}$ and *Nfkbiz*$^{-/-}$*Rag2*$^{-/-}$ mice (n = 10), together with those of *Nfkbiz*$^{-/-}$ mice (n = 30), are shown. Incidence of the disease (score ≥ 1) is expressed as a percentage. The disease scores are shown as mean ± SD.

(C) Histology of the periocular skin and conjunctiva of a 4-month-old *Rag2*$^{-/-}$ and *Nfkbiz*$^{-/-}$*Rag2*$^{-/-}$ mice. Sections of periocular skin and conjunctiva were stained with HE.

See also Figure S2.

Th17 cell-type response, was activated in the spleen and the cervical lymph nodes (Figure S1L), a result consistent with the previous finding that IκB-ζ is required for efficient Th17 cell differentiation (Okamoto et al., 2010). Furthermore, the number of CD138$^+$ plasmacytes was increased in the lymph nodes (Figure S1M). Accordingly, serum concentrations of various immunoglobulin subtypes were elevated in *Nfkbiz*$^{-/-}$ mice (Figure S1N).

In order to evaluate the roles of lymphocytes in the inflammatory response, we generated *Nfkbiz*$^{-/-}$*Rag2*$^{-/-}$ mice. In *Nfkbiz*$^{-/-}$*Rag2*$^{-/-}$ mice lacking mature lymphocytes (Shinkai et al., 1992), inflammation was dramatically alleviated (Figure S2). The incidence of the disease was much lower than in *Nfkbiz*$^{-/-}$ mice, and the onset and progression of the inflammation were substantially delayed (Figures 2A and 2B). Histopathological analysis of the periocular skin and the conjunctiva in 12-week-old *Nfkbiz*$^{-/-}$*Rag2*$^{-/-}$ mice did not reveal any infiltrating cells or any other signs of inflammation (Figure 2C). Taken together, these observations indicated that activated lymphocytes are essential for the initiation and/or progression of inflammation.

Inflammation in IκB-ζ-Deficient Mice Is Caused by an SS-like Autoimmune Disease

Because lymphocytes play a critical role in inflammation, we next examined the presence of autoantibodies in *Nfkbiz*$^{-/-}$ mice. Immunohistochemical studies showed that serum from *Nfkbiz*$^{-/-}$ mice, but not wild-type mice, reacted with the nuclei of cells in the skin (Figure 3A). Consistent with this finding, we detected high titers of anti-nuclear antibody in *Nfkbiz*$^{-/-}$ mice (Figure 3B).

Because inflammation in the mutant mice was always initiated in the periocular regions, we carefully analyzed the periorbital tissues in *Nfkbiz*$^{-/-}$ mice. We found that the exorbital lacrimal glands in *Nfkbiz*$^{-/-}$ mice exhibited inflammation characterized by a periductal infiltration of CD4$^+$ T cells and B cells (Figure 3C). Reduced tear secretion was also observed in *Nfkbiz*$^{-/-}$ mice (Figure 3D). Because these symptoms are a hallmark of SS, we measured the diagnostic markers of SS. As anticipated, high titers of both SSA and SSB antibodies, which are sensitive and specific to primary SS, respectively (Vitali et al., 2002), were detected in the sera of *Nfkbiz*$^{-/-}$ mice (Figures 3E and 3F). Furthermore, aged *Nfkbiz*$^{-/-}$ mice often exhibited interstitial pneumonia, a frequent complication of SS (Figure 3G; Table S1). Collectively, these observations indicate that IκB-ζ-deficient mice develop an SS-like autoimmune disease.

IκB-ζ Deficiency in Hematopoietic Cells Is Not Essential for SS-like Inflammation

To further investigate the roles of IκB-ζ-deficient lymphocytes, we adoptively transferred splenocytes prepared from wild-type (+/+) or *Nfkbiz*$^{-/-}$ (−/−) mice to either *Nfkbiz*$^{+/+}$*Rag2*$^{-/-}$ (+/+) or *Nfkbiz*$^{-/-}$*Rag2*$^{-/-}$ (−/−) recipient mice (Figures 4A and S3A). As expected, adoptive transfer of *Nfkbiz*$^{-/-}$ (−/−) splenocytes to *Nfkbiz*$^{-/-}$*Rag2*$^{-/-}$ (−/−) recipient mice (−/− → −/− in Figure 4A) elicited severe periocular inflammation, as in *Nfkbiz*$^{-/-}$ mice. Surprisingly, wild-type (+/+) splenocytes induced heavy inflammation when transferred to *Nfkbiz*$^{-/-}$*Rag2*$^{-/-}$ (−/−) recipient mice (+/+ → −/−) as well as *Nfkbiz*$^{-/-}$ (−/−) splenocytes. Transfer of purified wild-type T cells, but not B cells, induced ocular inflammation in *Nfkbiz*$^{-/-}$*Rag2*$^{-/-}$ (−/−) recipient mice (Figure 4B). Furthermore, purified wild-type CD4$^+$ T cells alone were sufficient to induce inflammation. In contrast, *Nfkbiz*$^{-/-}$ (−/−) splenocytes did not elicit any inflammation in *Nfkbiz*$^{+/+}$ *Rag2*$^{-/-}$ (+/+) recipient mice (−/− → +/+). Thus, whereas the presence of lymphocytes is essential for inflammation, IκB-ζ deficiency in lymphocytes is not required for the development of the disease. Consistent with this conclusion, fetal liver transfer from *Nfkbiz*$^{-/-}$ mice to lethally irradiated wild-type mice did not elicit inflammation (Figures S3B and S3C), further excluding a principal role for IκB-ζ-deficient hematopoietic cells in eliciting inflammation.

To identify the IκB-ζ-deficient cells responsible for the inflammation, we generated *Nfkbiz*$^{flox/flox}$ mice, in which exons 5–7 of the *Nfkbiz* gene were flanked by *loxP* sites, by gene targeting with C57BL/6-derived embryonic stem cells (Figures S4A–S4C). At first, we crossed the *Nfkbiz*$^{flox/flox}$ mice with CAG-Cre transgenic mice (Sakai and Miyazaki, 1997) to create mice lacking IκB-ζ in the whole body on the C57BL/6 background (referred to as *Nfkbiz*$^{\Delta/\Delta}$). The *Nfkbiz*$^{\Delta/\Delta}$ mice developed SS-like dacryoadenitis, conjunctivitis, and periocular dermatitis in common with *Nfkbiz*$^{-/-}$ mice, which were on the 129Sv-C57BL/6 mixed background (Figures S4D–S4F).